Daniel de Melo Pereira

# A soft lithography method for patterning calcium phosphate ceramics

September 2014

· U  C ·

UNIVERSIDADE DE COIMBRA

Daniel de Melo Pereira

# A soft lithography method for patterning calcium phosphate ceramics

*Dissertação apresentada à Universidade de Coimbra para cumprimento dos requisitos necessários à obtenção do grau de Mestre em Engenharia Biomédica*

Supervisors:
Hermínio José Cipriano de Sousa (CIEPQPF, DEQ, Universidade de Coimbra)
Mara Elga Medeiros Braga (CIEPQPF, DEQ, Universidade de Coimbra)
Pamela Habibovic (MIRA,  University of Twente)

Coimbra, 2014

This work was done in collaboration with:

University of Twente

# UNIVERSITY OF TWENTE.

MIRA – Institute for biomedical technology and technical medicine

**MIRA**
BIOMEDICAL TECHNOLOGY
AND TECHNICAL MEDICINE

v

# ACKNOWLEDGEMENTS

I would like to extend my gratitude to everyone that, in some way or another, contributed to the development of this work.

To my supervisors from Universidade de Coimbra, Hermínio de Sousa e Mara Braga, thank you for the enthusiasm and for a great learning environment provided, and also for the opportunity to explore the world of academic research.

To my supervisor from University of Twente, Pamela Habibovic, for the opportunity to join her research group, and especially for always giving room for discussing ideas with an open mind. Thank you also to the other members of the group, Niloofar, Ana, Zyrian, Barbara, Alessandro and Angad, for the enjoyable working environment, and availability to help.

To David Barata, my daily supervisor in the lab, for the countless hours, invaluable support, the outstanding ability to think outside the box and inspire me to look further.

To Alessandro Resmini, for much time devoted exploring the patterning technique.

To my fellow students at the master table, thank you for the shared moments, from lab work to lunches and borrels.

A special thank you to my Calslaan family, I could not have done it without you.

To my parents.

# ABSTRACT

A soft lithography method based in micromoulding in capillaries was used for patterning calcium phosphate ceramics on silicon substrates, by the nucleation and growth of crystals from a supersaturated solution of calcium and phosphate ions infiltrated in microchannels. The microchannels were defined by a PDMS mold, obtained from casting on silicon masters of different patterns, and the underlying silicon substrate.

Infiltration efficiency of the solution by capillary forces was tested on two categories of patterns, network-like channels and parallel channels, with the latter showing complete infiltration for channel length up to 1 cm, for plasma treatment time of 1 min to the PDMS mold and Si substrate. The deposited material consisted of radial nodes of elongated needle-like crystals, which were observed in regions ranging from high nucleation density and limited crystal growth to low nucleation density and extensive growth.

The crystalline phase was identified by X-ray diffraction as di-calcium phosphate anhydrous (DCPA) and beta tri-calcium phosphate ($\beta$-TCP) upon heat treatment of substrates at 950ºC for 3 hours.

The pattern confinement and calcium and phosphorus distribution inside the channel were assessed by electron dispersive spectroscopy. Calcium and phosphate ion release profiles were obtained, and it was found that ionic concentration did not significantly changed in cell culture conditions for 7 days. Morphology of the ceramic pattern was not significantly altered after ageing in cell culture medium for 3 days.

Biocompatibility of the Si-CaP substrates and cell proliferation were assessed by viability and DNA quantification assays. An increase in metabolic activity was seen over the 7 days, but low DNA content indicated low cell numbers at days 1 and 3, suggesting hindered attachment on the Si-CaP samples.

Scanning electron microscopy and fluorescence imaging of F-actin showed that cells stretch and align in the direction of patterned lines, with stronger orientation observed on narrower lines (1 to 10 um) as compared to wider lines (20 to 80 um). Vinculin was found dispersed in the cytoplasm, while focal adhesion kinase was sometimes concentrated on attachment points along the edge of cells cultured on the Si-CaP substrates at 3 days, possibly indicating formation of focal adhesions to the ceramic substrate.

Crystal growth dynamics were observed in real-time with a modified mini incubator and time-lapse microscopy, and this platform showed promising results for the study of crystal growth dynamics in confined spaces.

x

# RESUMO

Uma técnica inspirada na micromoldagem em capilares foi adaptada para produzir padrões de cerâmicos de fosfato de cálcio num substrato de silício, através da nucleação e crescimento de cristais a partir de uma solução supersaturada de iões de cálcio e fosfato. A solução foi infiltrada em microcanais definidos pelo molde de PDMS e pelo substrato de silício.

A eficiência de infiltração por capilaridade foi testada em duas categorias de padrões, nomeadamente padrões de canais interconectados, e padrões de canais paralelos. A infiltração nos padrões de canais paralelos foi completa para um comprimento do canal até 1 cm, e para um tratamento de plasma de 1 min ao molde e ao substrato.

O material depositado foi composto por nodos radiais de cristais alongados semelhantes a agulhas, que foram observados em regiões de densidade de nucleação elevada e crescimento cristalino limitado ou em regiões de densidade de nucleação baixa e crescimento cristalino extensivo. A fase cristalina foi identificada por difracção de raios-X como fosfato de di-cálcio desidratado (DCPA - di-calcium phosphate anhydrous) que mudou de fase para fosfato de tri-calcium beta (β-TCP - beta tri-calcium phosphate) quando as amostras foram sujeitas a um tratamento térmico a 950°C durante 3 horas.

O confinamento do material depositado, e a distribuição de cálcio e fósforo dentro dos canais foi analisada por espectroscopia de dispersão de electrões. Foram obtidos perfis de libertação para o cálcio e fosfato, em meio de cultura de células, e não foram encontradas diferenças significativas na concentração iónica após 7 dias. A morfologia dos padrões não foi alterada significativamente após envelhecimento em meio de cultura por 3 dias.

A biocompatibilidade dos substratos e proliferação celular foi avaliada com testes de viabilidade e quantificação de DNA. Foi observado um aumento de actividade metabólica ao longo dos 7 dias, mas a quantidade baixa de DNA nos dias 1 e 3 sugerem dificuldades de adesão ao substrato.

Foi mostrado por microscopia de varrimento electrónica e immunofluorescência dos filamentos de actina que as células se apresentam esticadas e alinhadas na direcção dos padrões de linhas, e este efeito é mais pronunciado nas linhas mais estreitas (1 a 10 μm) do que nas linhas mais largas (20 to 80 μm). Vinculina foi encontrada dispersa no citoplasma, enquanto a cinase de adesão focal foi observada por vezes concentrada em pontos de adesão situados na orla das células, indicando a possível formação de adesões focais no material cerâmico.

A dinâmica de crescimento dos cristais foi observada em tempo real com uma mini câmara de incubação e microscopia de time-lapse, e esta plataforma mostrou resultados promissores para o estudo de crescimento de cristais em espaços confinados.

# Table of contents

# 1. INTRODUCTION

## 1.1. Tissue Engineering

The concept of building artificial body parts has been present in many aspects of human culture long before it had any practical application. It is related to a quest for longevity that has accompanied humankind from its very beginning, but only relatively recently did our ingenuity enabled us to start making the first steps in that great challenge, that is to ultimately be able to engineer a whole organ for implant in a human patient (Vacanti & Vacanti 2007).

The necessity stems from a lack of alternatives to tissue or organ transplantation, the standard solution for organ failure due to disease or traumatism, which is one of the many problems that an over-aged population faces in developed countries (Cohen 2003; Lloyd-Sherlock 2000). Organ transplant has the known drawbacks of limited availability due to donor scarcity, resulting in long waiting lists for patients so that the majority of candidates never gets a chance at transplant (Matesanz 2013); and immunologic complications that can result in the rejection of implanted tissue (Ingulli 2010). Bone is currently the second most transplanted tissue (Shegarfi & Reikeras 2009) and there is a great demand for tissue engineered solutions for bone related problems, for example defects caused by trauma, tumours, osteoporosis or other disorders (Habibovic & Groot 2007; Liu *et al*. 2013).

The multidisciplinary field of Tissue Engineering set the objective of finding adequate artificial replacements for the standard autologous or allogeneic tissue used in transplant procedures. These artificial implants should either replace the function that was lost, or enable and enhance the regeneration of the affected tissue. For this purpose a range of materials can be used in combination with cells and soluble factors to build an artificial construct that is able to fulfil all the requirements necessary for the successful recovery of normal tissue function (Langer & Vacanti 1993). The engineering of such a construct has many aspects to be considered, but central to all considerations are the biomaterials that make up the supporting matrix – or scaffold – for it is on them that depend three broad categories of functions: the tri-dimensional shape and volume of the construct, the transduction of signals exogenous to the cells that populate the scaffold and the ability to sustain those cells and direct them to form new tissue (Williams 2008).

## 1.2. Bone tissue engineering

Bone is a dynamic living tissue, composed, like any other, by cells and extracellular matrix. Its cellular components are osteoblasts that secrete components of the extracellular matrix, osteocytes that reside in lacunae surrounded by mineralized matrix, and osteoclasts that are responsible for bone resorption. There are also osteoprogenitor cells that line the inner and

outer surface of bone tissue and differentiate in osteoblasts when activated. The extra-cellular matrix of bone is mineralised, consisting in an organic phase (around 25% in weight) of mostly collagen (around 90%) and non-collagenous proteins (around 10%) and an inorganic phase (around 65% in weight – water makes up for the rest) that consists of poorly crystalline carbonated hydroxyapatite, mineralized within and around the collagen fibrils. This collagen-hydroxyapatite composite is organised into two macroscopically distinct types of bone, cortical bone and cancellous bone. Cortical bone is compact and dense, while cancellous bone is porous and biologically more active – it houses the bone marrow and undergoes constant remodelling by osteoblasts and osteoclasts. Their mechanical properties are very different, for example the elastic modulus is between 15 to 20 GPa for cortical bone and between 0.1 and 2 GPa for cancellous bone. A specific bone will have mechanical properties that depend on the relative distribution and presence of both types of bone tissue. (Bala *et al*. 2013; Rho *et al*. 1998; Olszta *et al*. 2007; Bala *et al*. 2011).

The highly organized and anisotropic structure of bone presents a challenge for the design of scaffolds for tissue engineering, but some features are generally recognised as desirable for a bone TE scaffold and its constituting materials: a tri-dimensional network of interconnected macro (200-350 µm) and micro (less than 20 µm) pores is essential for cell proliferation, formation of new tissue and angiogenesis, as well as adequate nutrient distribution along the scaffold; bulk mechanical properties matching those of the surrounding tissue, and tolerance of those properties to the remodelling processes of bone; biocompatible and bioresorbable materials with a degradation and resorption rate matching the formation and maturation of new tissue and structural and chemical surface features that, while consistent with the others already described, also elicit the appropriate response from cells, guiding them to proliferate through the scaffold (osteoconduction) and inducing the differentiation of cells that are not committed to the osteogenic lineage into osteoprogenitor cells – a property known as osteoinduction; (Woodruff *et al*. 2012; Gao *et al*. 2014; Hutmacher 2000; Liu *et al*. 2013; Habibovic & Groot 2007; Bose *et al*. 2012).

Traditional biomaterials used in long-term implants, e.g., titanium alloys, are not suitable for applications in tissue regeneration since their only requirement is to be as inert as possible and thus achieve long term biocompatibility within the host tissue (Williams 2008). Much more is asked of a material involved in tissue regeneration, and this supports the need for investigation of innovative biomaterials capable of such demanding functions.

## 1.3.  Biomaterials

The design of new biomaterials for tissue engineering is moving towards controlling the biological response induced by them in vivo (Ratner & Bryant 2004; Williams 2009; Brown &

Badylak 2013; Place *et al*. 2009). There are two main objectives, on one hand the minimization of unfavourable responses from the host tissue, such as inflammation, non-specific protein adsorption, foreign body reaction and fibrous capsule formation (Anderson 2001; Anderson *et al*. 2008); and on the other hand the appropriate signalling for cells from the surrounding tissue to engage in pathways that lead to regeneration (Ratner & Bryant 2004).

In the case of biomaterials for bone tissue engineering, bioactivy is often related to their osteoinductive potential, already described as the ability to recruit undifferentiated cells to the osteogenic lineage. Osteoinductivity is evaluated by the formation of heterotopic bone *in vivo*. A reliable and generic *in vitro* screening test for the osteoinductive behaviour of biomaterials *in vivo* has yet to be found, but a model with human bone marrow stromal cells (hBMSC) was able to correlate the expression of osteogenic genes *in vitro* with the ectopic formation of bone in sheep for four different types of calcium phosphate ceramics (Yuan *et al*. 2010), showing that it may be a good candidate for such a screening.

Some examples of osteoinductive materials, as reviewed by Barradas *et al.* (2011) include the notable calcium phosphate ceramics (CaP) such as hydroxyapatite (HA), β tricalcium phosphate (β-TCP), biphasic calcium phosphate (BCP - a mixture of HA and β-TCP), dicalcium phosphate anhydrous (DCPA), dicalcium phosphate dihydrate (DCPD), carbonated apatite (cHA), calcium pyrophosphates (CPP), a mixture of HA and calcium carbonate. Some examples of commercially available bone graft and implant products based on CaP ceramics are presented in Figure 1. There are also examples other than ceramics, such as poly-HEMA, porous titanium, and composites of polylactide and HA particles or CaP coated titanium that are found to be osteoinductive.



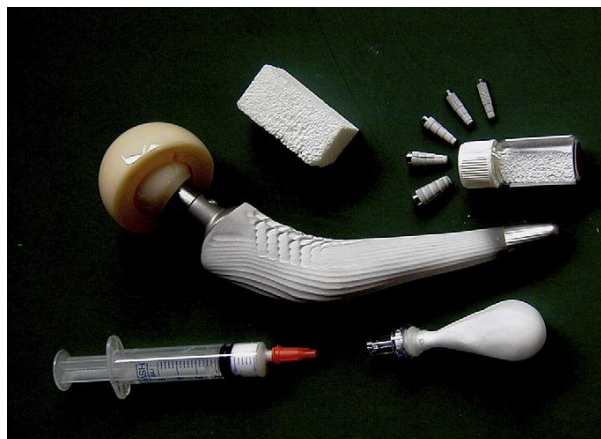Figure 1. Some examples of calcium-phosphate based materials used in applications for bone grafts and implants. Reproduced from Dorozhkin (2010).

Despite the mounting examples of osteoinductive materials, the underlying biological mechanisms are still poorly described. They all have in common the formation of a biological carbonated apatite layer upon implantation. There is evidence of chemistry playing a role,

specifically the presence of calcium phosphates and their availability to the physiological environment, but the macrostructure of the material, in terms of porosity and geometry, also has an effect on bone formation, as well as micro- and nanoscale surface features (Barradas *et al.* 2011). In a study comparing the osteoinduction potential of different CaP ceramics, two BCP materials (80 to 20 %wt HA:β-TCP) with different surface specific area (0,2 and 1,5 m$^2$/g) were implanted heterotopically, and only the BCP with higher surface specific area was osteoinductive, showing that porosity is highly desirable characteristic. On the other hand, when HA was compared to BCP with similar surface specific area, only BCP resulted in ectopic bone formation, showing that the presence of a more soluble CaP phase such as β-TCP to be critical for the osteoinductive process. The knowledge of how these material properties influence osteoinduction is growing, but still falls short of the desired level of control over the host response to an implanted biomaterial. It must also be noted that osteoinduction is but one aspect of bioactivity. There are others to look into, such as the profile of adsorbed proteins on the biomaterial, and the influence of surface chemistry and micro- and nano-topography on the host immune response (Brown & Badylak 2013; Bruinink *et al.* 2013).

# 1.4. Cell-material interaction

The surface of the biomaterial plays an important role as interface between the cell and the material, and knowledge of the interaction between them is crucial to the development of new biomaterials.

## 1.4.1. Surface topography

Topography characteristics such as roughness, morphology, geometry and degree of organization have been shown to influence cell adhesion, proliferation and differentiation in a number of ways. It is well established that the proliferation and differentiation potential of osteosarcoma-derived cells, MG-63, can be induced by surface roughness, although adhesion is lower on rougher substrates (Kieswetter *et al.* 1996; Lincks *et al.* 1998; Brett *et al.* 2004; Hamilton & Brunette 2007). Another example correlates adhesion of human osteoblasts with parameters that describe degree of organization instead of amplitude of roughness (Anselme *et al.* 2000) Specifically, cells cultured on less organized surfaces (sandblasted) exhibited lower adhesion. Dalby *et al.* showed that the organization level of nano pits had an effect on the production of osteopontin and osteocalcin by osteoprogenitor cells, and on the differentiation of mesenchymal stem cells towards osteogenic lineage (Dalby *et al.* 2007). There are many examples of cell alignment by contact guidance on grooved substrates (Lamers *et al.* 2010; Biggs *et al.* 2008; Nadeem *et al.* 2013; Prodanov *et al.* 2010). More recently, a porous honeycomb patterned surface of polystyrene was shown to induce differentiation of human

mesenchymal stem cells (hMSC) towards the osteogenic or myogenic lineage, depending on the pore size (Kawano *et al.* 2014).

### 1.4.2. Surface chemistry

Material surface chemical characteristics such as functional groups, surface charge and degradation products also influence cell behaviour. Cell adhesion and proliferation depend on the hydrophilic/hydrophobic balance at the surface and also on the chemical composition. Generally, cells prefer moderate to highly hydrophilic surfaces (water contact angle between 40-70) (Anselme *et al.* 2010; Oliveira *et al.* 2014; Arima & A 2007), although the interplay of wettability/chemistry is not very clear: one study found similar proliferation rates of MG-63 cells on –OH, –NH$_2$ and –CH$_3$ terminated self-assembled monolayers (SAM) despite the difference in water contact angle (respectively 11º, 54º and 76º) (Schweikl *et al.* 2007).

Surface charge, measured by zeta potential, was shown to influence the differentiation of osteoblasts on a polylactide-CaP composite (Moller *et al.* 1994).

Protein adsorption also depends on the surface chemistry and topography, the surface is only sensed by cells through a layer of water and adsorbed proteins that settle on the first instants of contact (Anselme *et al.* 2010). A study on the adsorption of collagen to a combination of smooth ($R_a = 0.5$ nm) or rough ($R_a = 4.8$ nm), hydrophilic (–OH terminated) or hydrophobic (–CH$_3$ terminated) surfaces found differences in the amount of adsorbed collagen on substrates with different functional groups (larger amount on hydrophobic surface), but no difference for substrates with different roughness. The supra-molecular organization of collagen fibres however, was shown to be dependent both on chemistry and topography (Denis *et al.* 2002).

In cell culture or in a real implant situation, synergy between physical and chemical cues provides complex signalling to cells. From the perspective of design of new biomaterials it is interesting to decouple the influence of different surface cues on cell behaviour, and how to do it has been a fundamental topic in biomaterials research (Yao *et al.* 2013a).

## 1.5. Biomaterial patterning as a tool to study cell interactions

With the development of surface patterning methods it became possible to design complex substrates with defined chemical and geometrical parameters, effectively decoupling chemistry from topography, and allowing to ascertain the respective influence on cell adhesion, proliferation, communication and differentiation (Yao *et al.* 2013a; Nikkhah *et al.* 2012; Zheng *et al.* 2013; Falconnet *et al.* 2006). Soft lithography based techniques of micropatterning for cell studies are abundant since Whitesides built on the classical photolithography from

microelectronics (Xia & Whitesides 1998). In general, it involves the use of an elastomeric stamp or mold to transfer an embossed pattern to other surfaces. It is less expensive than photolithography because it does not require the technological apparatus usually kept in a cleanroom or the manufacture of a photomask, has the advantages of providing control over surface chemistry, the possibility of application to non-planar substrates and a wider range of materials than photolithography (Xia & Whitesides 1998). The most common techniques for surface patterning are microcontact printing (μCP) (Kumar & Whitesides 1993), replica molding (REM) (Xia *et al*. 1997), microtransfer moulding (μTM) (Zhao *et al*. 1996), micromoulding in capillaries (MIMIC) (Kim *et al*. 1995), solvent-assisted micromoulding (SAMIM) (Kim *et al*. 1997), cast moulding (Terris *et al*. 1996) and microfluidic patterning (Folch *et al*. 1999; Li *et al*. 2007). Many aspects of cell-material interaction have been evidenced thanks to material patterning technologies, as reviewed by Yao *et al* (2013).

## 1.5.1. Structural patterning

Some effects of topography on cell behaviour were already mentioned, but here are a couple of examples that have patterning as the underlying technique. Patterned ridges with different groove width revealed an effect on NIH 3T3 fibroblasts migration speed and degree of orientation with the substrate (Kim *et al*. 2009). By varying the height of a square grid pattern from 1 μm to 2 μm, mouse mesenchymal stem cells (b) consistently changed the location of their focal adhesions from the top of the pattern to the square bottoms, while the size of focal adhesions increase with the rigidity of the substrate (Seo *et al*. 2013). On the differentiation of murine MSC, a 3 μm pattern interval showed the highest expression of osteogenic markers (Seo *et al*. 2011). Flexible pillar arrays produced by replica moulding were employed to study cell mechanics (Tan *et al*. 2003), and hMSC differentiation (Fu *et al*. 2010).

A high-throughput screening platform for studying the influence of randomly designed surface topography features on proliferation and differentiation of hMSC using virtually any fluorescence based staining was designed, and osteogenic differentiation assessed by alkaline phosphatase staining on more than 2000 different topographies, illustrating the power of this method (Unadkat *et al*. 2012)

An innovative approach to transfer 2D patterns into tri-dimensional structures by a combination of standard photolithography with thermoforming of polymers resulted in microcavities (300 μm deep, 350 μm wide) with patterned topographies, platforms that could be useful to study cell interaction in a 3D environment (Giselbrecht *et al*. 2011).

## 1.5.2. Patterning of biomolecules

Micropatterning of a Arg-Gly-Asp peptide (RGD) on a non-fouling poly(ehthyleneglycol) (PEG) background was used to discover critical areas of cell spreading for mouse osteoblastic cell line MC3T3-E1, such as the critical area to go from apoptosis to growth (64 $\mu m^2$), or critical areas for the occupation by more than 1 cell (335 $\mu m^2$) (Yan *et al*. 2011). The same patterning technique was used to study the effect of cell shape on differentiation of mouse MSC, with circular and star shapes having the best results towards the adipogenic and osteogenic lineage, respectively (Peng *et al*. 2011). Using the same star shape but with different subcellular edge curvatures (convex versus concave), it was observed that cells with concave curvature, correlated with more actomyosin contractility, were more likely to become osteoblasts (Kilian *et al*. 2010). A correlation between cellular aspect ratio and osteogenic differentiation of mouse MSC was found to be non-monotonic, but with a peak of ALP activity for an aspect ratio of 2 (Peng *et al*. 2011) a result later confirmed in the absence of induction medium (Yao *et al*. 2013b). The biological pathways of osteogenic differentiation through cell shape, specifically aspect ratio, were then related to the cell-tension pathway RhoA-ROCK (McBeath *et al*. 2004) and it was shown, using patterned polyacrylamide hydrogels, that cell tension, related to osteogenic differentiation, peaked for an aspect ratio of 2.8 for NIH 3T3 cells (Rape *et al*. 2011). Osteogenic or adipogenic differentiation of rat MSC (Peng *et al*. 2011) and human MSC (Song *et al*. 2011) was correlated with cell spreading size, with larger cell size preferred for osteogenic differentiation, and this was shown with the same RGD on PEG patterning method previously mentioned.

Also helpful in studying the interaction between cells is the design of patterns that control the number of cells in contact with each other. For example, the influence of cell aggregate number was found to play a role on rat MSC cultured under osteogenic or adipogenic induction media, larger aggregates showed increased differentiation for either fate when cultured in the respective medium, but a competition effect was noticed when cells were cultured under combined induction medium. In this case, osteogenic differentiation decreased with cell aggregate number although the adipogenic differentiation still increased monotonically (Peng *et al*. 2011).

## 1.5.3. Hydrophilic/hydrophobic patterning

A review on the cell interactions with superhydrophilic/hydrophobic surfaces by Oliveira *et al.* (2014) provides many examples of the patterning of materials with different wettability. For instance, patterns of hydrophilic HEMA-EDMA grafted with hydrophobic PFPMA at specific sites were proposed to study interactions between cells in co-culture (Efremov *et al*. 2013); the adhesion and proliferation of osteoblast-like SaOs-2 cells was studied

on patterned polystyrene (obtained by selective irradiation with UV-O$_3$) and spatial confinement was possible on the superhydrophilic regions (Oliveira *et al*. 2011).

### 1.5.4. Patterning of ceramics

For all these examples and others, there is an outstanding gap in micropatterning techniques related to ceramic materials, mainly due to the technical difficulties of handling ceramics below the 100 μm scale (Holthaus *et al*. 2011; He *et al*. 2014). There are, however, some methods able to pattern ceramics below 100 μm, such as micromachining and laser ablation, methods based on suspensions of ceramic particles and soft lithography (μTM and REM) or Aerosol-Jet printing (Holthaus *et al*. 2011), but of these only the microtransfer moulding and Aerosol-Jet printing produce thin films on a substrate. Functional oxides such as zirconia and zinc oxide can be patterned on silicon by a combination of sol-gel and MIMIC methods (Khan & Elshof 2012; Göbel *et al*. 2010), or by selective nucleation and growth on hydrophilic/hydrophobic patterns produced by channel diffusion of oxygen plasma and SAM templates (George *et al*. 2011) (Figure 2). Also of note are silica patterns produced by soft embossing of a sol-gel precursor and subsequent sintering (Pelaez-Vargas *et al*. 2013), and a method describing the patterning of hydroxyapatite on a PEG non-fouling background (He *et al*. 2014). Still, there is much room for improving methods for patterning of bioceramics such as calcium phosphates.
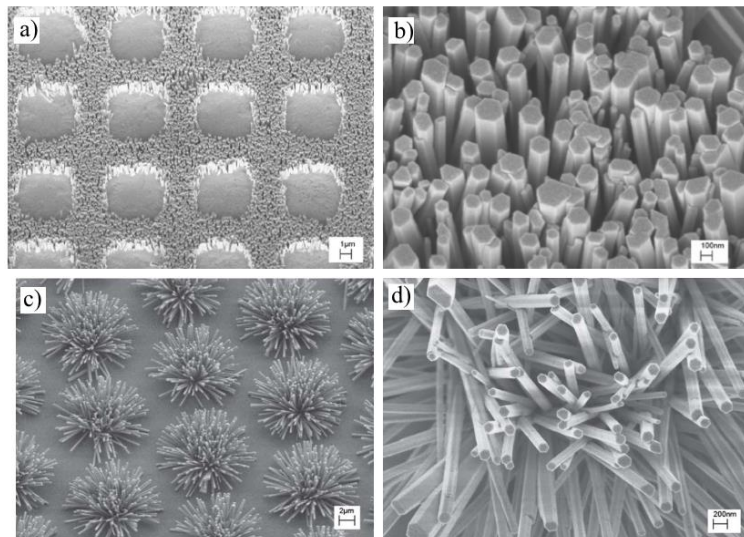


Figure 2. SEM micrographs of two examples of patterned zinc oxide (ZnO) nanowires, by electroless deposition on hydrophilic/hydrophobic patterns at a) low and b) high magnification (George *et al*. 2012) and ZnO nanowires grown from immersion of a polystyrene substrate patterned with ZnO seed sites in a mineral solution, at c) low magnification and d) high magnification (George *et al*. 2011).

## 1.6. Goals and motivation

The goal of the work here reported was to develop and optimize an economic and reliable patterning method for calcium phosphate ceramics that allowed control over structural properties and chemical nature of the deposited ceramic materials. Calcium phosphate ceramics are widely used in bone tissue engineering applications, owing to their resemblance with the mineral phase of bone, excellent biocompatibility and bioactive properties. Patterning of these materials provides a way to comprehensively address the study cell-material interactions in defined microenvironments, however it poses some technical challenges, especially below the 100 μm threshold.

By adapting a micromoulding in capillaries (MIMIC) method, inspired in previous work for patterning of functional oxides from George *et al.* (Figure 2), calcium phosphate patterns were obtained by infiltration of a supersaturated mineral solution into the confined spaces defined by a PDMS mould, with an embossed pattern, and a flat substrate.

Obtained ceramic patterns were also to be characterized in respect to their morphology, physicochemical properties and biocompatibility.

# 2. MATERIALS AND METHODS

## 2.1.    Materials

Polydimethylsiloxane (PDMS) Sylgard 184 elastomer kit was from Dow Corning, USA. Calcium nitrate $Ca(NO_3)_2 \cdot 4H_2O$, phosphoric acid $H_3PO_4$ 85 wt.% in H2O, Triton X-100, Tween-20, bovine serum albumin (BSA) and hexamethyldisilazane (HMDS) were obtained from Sigma-Aldrich, USA, and used without further processing. Phosphate buffered saline (PBS), Minimum Essential Medium α (α-MEM), fetal bovine serum (FBS) and trypsin were from Gibco, Life Technologies, USA. Fluorescein isothiocyanate (FITC) conjugated antibody for vinculin, focal adhesion kinase (FAK) rabbit antibody, F-actin probe Alexa Fluor 594 for phalloidin, secondary antibody Alexa Fluor 647 anti-rabbit and 4',6-diamidino-2-phenylindole (DAPI) were from Invitrogen, Life Technologies, USA. Presto Blue™ cell viability assay and CyQUANT™ cell proliferation assay were from Invitrogen, Life Technologies, USA. CDPstar 0.25 ready-to-use solution for ALP quantification was from Roche, Switzerland. QuantiChrom colorimetric kits for calcium (DICA-500) and phosphate (DIPI-500) ion quantification were from BioAssays Systems, USA. Human osteosarcoma cell line MG-63 (ATCC CRL-1427) was obtained from ATCC-LGC, United Kingdom.

## 2.2. Sample preparation and optimization

The sample preparation method is outlined in Figure 3.

PDMS molds were prepared by casting on silicon wafer master (Si-master) (Figure 3 steps i-iii). The Si-master was produced by the standard processes of photolithography followed by deep reactive ion etching (Adixen SE, Alcatel, France). PDMS was prepared by mixing the elastomer base and curing agent in a 10:1 ratio, and curing at 80ºC for 2 hours after casting on the Si master. The mold was peeled from the Si-master, patterns were manually cut from the replicated PDMS and carefully cleaned with nitrogen gas blow before conformal contact with an oxidized silicon piece (6 μm amorphous silicon dioxide layer), previously cut to match the mold size. Quality of contact was assessed by observing the color change at the PDMS – substrate interface. The mold and substrate were subjected to air plasma (Figure 3 step iv.b) (PDC-002 from Harrick Plasma, USA), or alternatively, the PDMS mold was subject to air plasma before conformal contact with the Si substrate (Figure 3 step iv.a). Channels were subsequently infiltrated with a supersaturated solution of calcium and phosphate ions (step v). This solution was prepared by mixing two precursor solutions, one (A) of 1 M calcium nitrate in 50% ethanol and the other (B) of 0,67 M phosphoric acid in 80% ethanol, yielding a final solution with a calcium to phosphate ionic ratio of 1.5. The two precursor solutions were prepared each in a 50 mL volumetric flask, and stored at 4 ºC in 125 mL plastic bottles. Prior

infiltration, 2 mL of each solution were filtered through a 0.2 μm Nalgene® syringe (SFCA filter) onto a 10 mL falcon tube, and agitated for homogeneity.

Infiltration was performed on both sides of the open channels by pipetting a droplet at the entrance of the channels and leaving it to homogenize overnight before drying in a hotplate at 60 ºC for 6 hours (Figure 3 step vi). The PDMS mold was then peeled from the Si substrate, revealing the deposited CaP pattern. These samples are referred to as Si-CaP (Figure 3 step vii). Further heat treatment was applied at 950 ºC for 3h.

A library of patterns[1] was available to test infiltration and consistency of CaP pattern formation. These were grouped in two categories, interconnected network of spaces or longitudinal channels. For each pattern, air plasma time was adjusted, and infiltration was described as complete or incomplete. After drying, clean peeling of the PDMS was assessed qualitatively by the force necessary to remove it and visible debris left behind. Iteration of this process led to adjusting the appropriate plasma time for complete infiltration in each pattern. It must also



Figure 3. Schematic of the patterning method.

be noted that at the onset of experimental work, a number of attempts were made with solutions of different composition, plasma treatments and drying conditions. These were not characterized extensively and are detailed in appendix 6.2.

## 2.3. Characterization

The morphology of patterns was analyzed by Scanning Electron Microscopy (SEM; Philips XL-30, Netherlands), Si-CaP samples were gold coated by sputtering (30 mA) for 40 seconds in argon atmosphere. Elemental analysis was performed by Energy-dispersive X-ray spectroscopy (EDX; TEAM™ EDS system from EDAX, USA). Crystalline phase was identified by thin film X-ray diffraction (XRD) with X'Pert[3] Power diffractometer (Panalytical, Netherlands). Peak identification was made with the HighScore software.
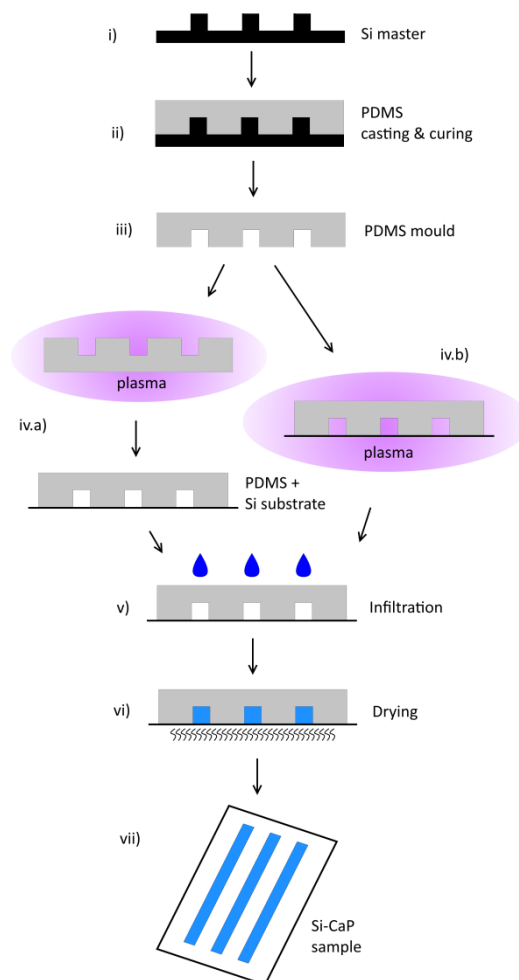
---

[1] SEM micrographs of the available silicon masters are presented in appendix 6.1.

## 2.3.1. Preparation of standard samples for cell culture and ion release

Silicon squared pieces of 2 cm side were prepared by cutting a 10 cm diameter wafer (6 μm oxide) in an automatic dicing saw system (DAD321, Disco, Japan). Breaking lines, 200 μm deep, were cut on the underside, in such a way to leave a $1cm^2$ central area (Figure 4).
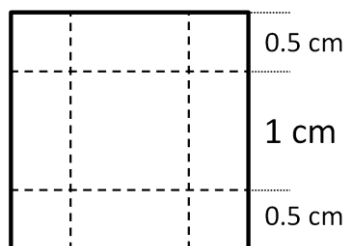


Figure 4. Schematic of breaking lines etched on the underside of the 2x2 cm silicon substrate.

Infiltration was performed on the 2 cm wide pieces, as described above, and after drying and annealing of respective samples, the borders were carefully broken by tweezers, to retain the central, more homogeneous area, and thus providing equally sized patterned Si-CaP samples for quantification of metabolic activity, DNA, ALP and ion release.

## 2.3.2. Calcium and phosphate ion release

Calcium ($Ca^{2+}$) and phosphate ($PO_4^{3-}$) ion release of the Si-CaP samples was quantified by the QuantiChrom colorimetric kits. The patterned Si-CaP samples used consisted of two different CaP phases (DCPA and β-TCP), and two different line widths of parallel lines, in this case 4 and 40 μm wide. Samples were in triplicate and the controls were incubation medium (same as used for cell culture) and a $H_2O$ blank (Table 1). The handling of the samples was kept the same as for the samples for cell culture, namely sterilization, working volumes, days before refreshing the medium and environmental conditions of incubation.

Table 1. Samples and controls for the calcium and phosphate release assay. Medium was refreshed on days 3 and 5, samples were collected on days 1,3 and 7. Basic Medium (BM) is the incubation medium described in the cell culture section.

| Sample | For each timepoint | |
|---|---|---|
| | DCPA | β-TCP |
| Si-CaP | 3 x 40 μm | 3 x 40 μm |
| | 3 x 4 μm | 3 x 4 μm |
| BM | 3 x | |
| H$_2$O | 3 x | |

The time-points for measurement were taken 1, 3 and 7 days of incubation. At these points, 1 mL of medium was collected and stored in the freezer at -30ºC, the rest of medium disposed of, and fresh medium added to the substrates. For the calcium assay, 5 μL of each condition and the standard curve (prepared in accordance with the kit's protocol) were pipetted into a transparent 96-well plate and incubated with 200 μL of working reagent (consisting of a

1:1 solution of reagents A and B, prepared before the assay) for 3 min. For the phosphate assay, samples were diluted 1:50 to fit the linear range of detection: 1 μL of each condition was pipetted into a transparent 96-well plate, together with 49 μL of de-ionized water. A de-ionized water control and a 30 μM $PO_4^{3-}$ standard from the kit were also measured. The samples were incubated with 100 μL of the working reagent for 30 min in the dark. The absorbance was measured at 612 nm and 620 nm, for $Ca^{2+}$ and $PO_4^{3-}$ respectively, in a microplate spectrophotometer reader (Multiskan™ GO, Thermo Fisher, USA).

# 2.4.  Cell culture

Prior to cell culture, for sterilization, all samples were washed two times with 70% ethanol for 5 min, one time with phosphate buffered saline (PBS) for 5 min, transferred to new tissue culture treated plastic well plates, washed again with PBS for 5 min, and left in incubation with medium for at least 30 min before aspiration and cell seeding.

Human osteosarcoma cell line MG-63 was used with Minimum Essential Medium α (α-MEM) supplemented with 10% fetal bovine serum (FBS), 1% penicillin and streptomycin and 1% L-glutamine. Cells were cultured at 37 ºC in a humidified atmosphere of 5% $CO_2$. Medium was replaced every 2 or 3 days. Upon reaching 80-90% confluence, cells were trypsinized with 0.25% trypsin in ethylene-diamine-tetraacetic acid (EDTA) for 5 minutes at 37 ºC. Trypsin was inactivated with three times the volume of medium, and sub-cultured in standard culture flasks or seeded for experiments. In all experiments, MG-63 cells were seeded at a density of 7500 cells/cm², in a working volume of 1.5 mL for 24-well plates and 2.5 mL for 12-well plates.

## 2.4.1. Biocompatibility and proliferation

Presto Blue™ cell viability assay was used to quantitatively measure cell metabolic activity. DNA quantification was performed with the CyQUANT™ cell proliferation assay. Patterned Si-CaP samples consisted of two different CaP crystalline phases – dicalcium phosphate anhydrous (DCPA) and beta tricalcium phosphate (β-TCP) – and different patterns – parallel lines with channel width and spacing of 80, 20 and 5 μm. Controls were silicon substrates without CaP pattern and tissue culture plastic (TCP). Samples are detailed in Table 2.

Table 2. Samples and controls for Presto Blue and DNA/ALP. TCP stands for tissue culture plastic.

| Sample | For each timepoint | |
|---|---|---|
| | DCPA | β-TCP |
| Si-CaP | 3 x 80 μm<br>3 x 20 μm<br>3 x 5 μm | 3 x 80 μm<br>3 x 20 μm<br>3 x 5 μm |
| Si | 3 x flat | |
| TCP | 3 x flat | |

Cells were cultured as described above, and at each timepoint – days 1, 3 and 7 – the medium was removed, samples were washed once with PBS and transferred to a new well plate. They were left to incubate with the Presto Blue™ reagent (10% in medium) for 2 hours, in parallel with a control (medium without cells).

After incubation, an aliquot of 100 µL medium was drawn and transferred to a black 96-well plate, in duplicate. The plate was read for fluorescence (excitation at 560 and emission at 590 nm) in a spectrophotometer (Victor3, Perkin-Elmer, USA). These samples were then washed with PBS and kept at -30 ºC for posterior DNA/ALP quantification.

For DNA quantification, samples were incubated in 500 µL of lysis buffer containing ribonuclease (the buffer consisted of reagent B of CyQUANT™ kit, diluted 20 times in 180 mM NaCl, 1 mM EDTA solution, with posterior addition of 0,1% RNase) for 1 hour. After incubation, 100 µL of lysate were transferred to a black 96-well plate, together with 100 µL of a dye solution (0.5% reagent A from the CyQUANT™ kit in 180 mM NaCl, 1 mM EDTA) and incubated for 15 minutes, in the dark. A standard curve and controls (without DNA) were also prepared in parallel. Samples were measured for fluorescence in a spectrophotometer (Victor3, Perkin-Elmer, USA).

## 2.4.2. Osteogenic profiling

Alkaline phosphatase (ALP) was quantified with CDPstar® 0.25 mM ready-to-use solution (Roche, Switzerland). The same lysate from DNA quantification was used, 10 µL were transferred to a white 96-well plate together with 40 µL of CDPstar® 0.25 mM and left to incubate for 30 min in the dark. Samples were measured for luminescence in a spectrophotometer (Victor3, Perkin-Elmer, USA).

## 2.4.3. Cell morphology and attachment

Cell morphology and attachment were evaluated by a four channel fluorescence imaging of nucleus, F-actin, focal adhesion kinase (FAK) and vinculin. For structural confirmation, SEM images were also obtained. Si-CaP patterned samples were used, namely with β-TCP crystalline phase, of parallel lines in a gradient of 1 to 80 µm (1, 2, 3, 4, 5, 10, 20, 40, 80 µm) with a total area of 1,5cm$^2$. Cells were seeded and cultured on 24-well plates for 1 and 3 days, as described above. For imaging purposes all samples were done in duplicate. At each time point the medium was removed, samples were washed with PBS and fixed with 4% paraformaldehyde for 20 min at room temperature (RT).

For fluorescent staining, samples were washed twice with PBS, permeabilized with 0,1% Triton X-100 in PBS for 5 min, washed twice with 0,1% Tween-20 in PBS (PBST). They were incubated in blocking buffer (2% BSA in PBST) for 30 min, and subsequently incubated overnight with a fluorescein isothiocyanate (FITC) conjugated antibody for vinculin (1:750 in

blocking buffer) in combination with primary rabbit antibody for FAK (1:500 in blocking buffer). On the next day the samples were washed twice with PBST, incubated with F-actin probe Alexa Fluor® 594 phalloidin (1:40 in PBST) combined with secondary antibody Alexa Fluor® 647 anti-rabbit (1:400 in PBST) for 1 hour, washed twice with PBS and finally incubated with DAPI (1:100 in PBS) to stain the nucleus, for 15 min. Samples were washed again and left in PBS. All incubation periods with fluorescent dyes were at room temperature in the dark.

Cells were observed with a fluorescence microscope equipped with a mercury lamp (E600, Nikon, Japan), for lower magnification (10x), and with a BD Pathway 435 (BD Biosciences, USA), for higher magnification (20x). The absorption and emission spectra of the fluorophores, the emission spectrum of the Hg lamp and filters used are shown in appendix 6.3.

For SEM, samples were dehydrated in ethanol series – 50, 60, 70, 80, 90, 95, 100 (%) – for 20 minutes each, followed by 20 min in HMDS. After removal of HMDS they were left to dry overnight and were subsequently gold coated by sputtering.

### 2.4.4. Statistical analysis

Significant differences between averages were performed with one-way Analysis of Variance (ANOVA) with Tukey's multiple comparison post-test with a significance level of $p < 0.05$. This notation applies to all figures: * $p<0.05$, ** $p<0.01$, *** $p<0.001$.

## 2.5. Crystal growth

Samples for crystal growth analysis were prepared as described above, but on a glass substrate instead of silicon. Glass substrates and PDMS molds were subjected to air plasma for 1 min on high power setting (corresponding to maximum power, 30W) and bonded together with gentle pressure. The bonded glass-PDMS was placed in a mini incubator adapted to fit the sample and allow observation from below with an inverted microscope, as described by Harink *et al*., 2014. Temperature was set at 37 °C and the solution was infiltrated. Crystal growth was observed and recorded using time-lapse bright field microscopy with an inverted optical microscope (TS100, Nikon, Japan).

# 3. RESULTS AND DISCUSSION

## 3.1. Optimization of infiltration

A range of different patterns was available to be tested for infiltration efficiency and consistency of formation of calcium phosphate patterns. They are grouped in two categories: interconnected network of channels and longitudinal channels. Figure 5 shows SEM micrographs of Si masters of patterns representative of these two categories. The PDMS molds were cast from these masters and used for infiltration of the CaP solution, as described in the methods section, preceded by air plasma treatment of the PDMS mold and the Si substrate.
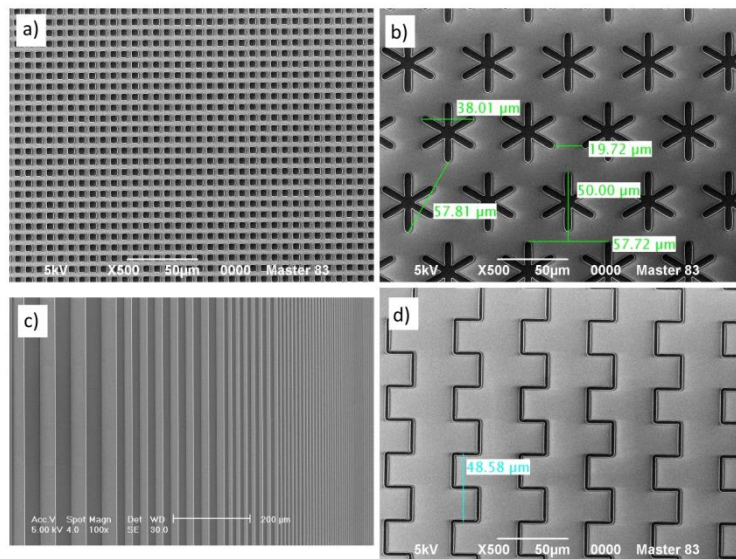


Figure 5. SEM micrographs of the silicon masters of representative patterns of two different categories: interconnected network of channels around a) squares (5 μm side) b) asterisks (50 μm diameter) or longitudinal channels of c) parallel lines (width ranging from 1 μm to 80 μm) or d) parallel lines with side reservoirs (45 μm width).

Results of the infiltration optimization on the two types of pattern are presented and differences between them discussed before proceeding to further characterization.

### 3.1.1. Interconnected network of spaces

Infiltration results for the interconnected spaces between squared pillars are presented in Figure 6. PDMS mold was prepared from the master in Figure 5a; the mold and Si substrate were subjected to 1 min air plasma treatment before infiltration, longer plasma times resulted in strong bonding of the PDMS to the silicon substrate (not shown). The solution that was infiltrated from the PDMS edge (dashed line in Figure 6a) towards the central region, showing an infiltration front, corresponding to the air-liquid interface, which penetrated on average 2 mm inside the mold (arrows in Figure 6a). The crystal morphology seemed independent of the squared spacers, with elongated crystals between 100 and 500 μm growing in every direction

(arrows in Figure 6b) between less organized areas. The elongated crystals can be seen at higher magnification (inset Figure 6b) appearing homogeneous with some gaps.
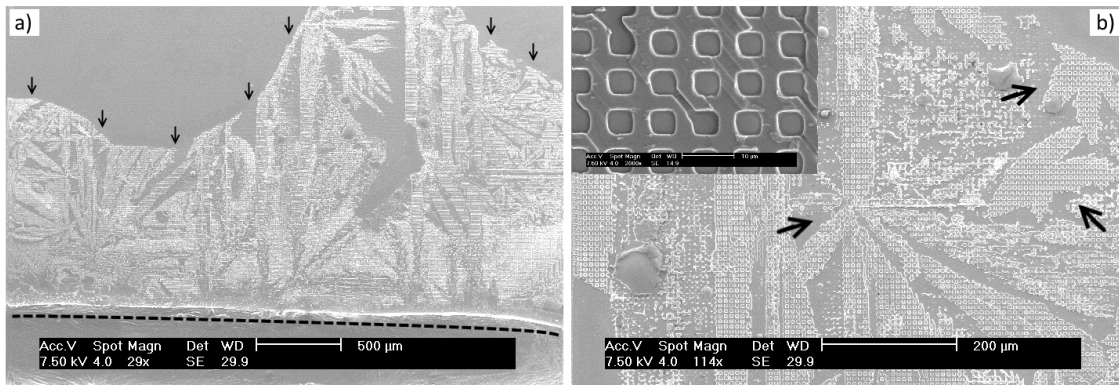


Figure 6. SEM micrographs of a Si-CaP pattern of squared pillars (5 µm side) at a) low magnification image of the pattern edge (dasehd line) and infiltration front (arrows) and close up of b) elongated crystals (arrows) amongst less organized areas; inset: high magnification of deposited material.

Infiltration results for the asterisk pattern are presented in Figure 7. PDMS mold was cast from the Si master in Figure 7b; plasma treatment of the mold and Si substrate was for 1 min. Elongated crystals between 100 to 500 µm grew from the edge of the pattern into the interconnected channels (arrows in Figure 7a) with empty spaces visible between them without visible deposits. Fewer elongated crystals were observed in the center of the mold, where the asterisks are surrounded by the deposited CaP material, without apparent organization (Figure 7b). In this case there is no infiltration front, as the mold was completely filled with solution.
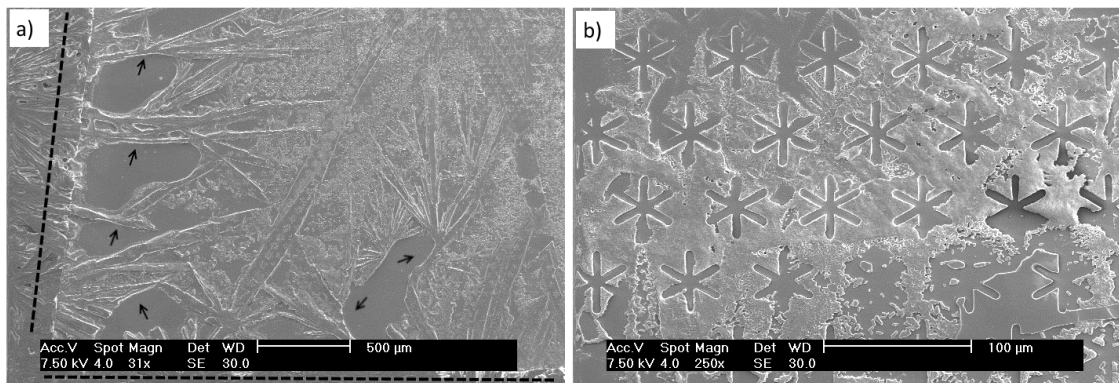


Figure 7. SEM micrographs of the asterisk pattern (50 µm radius); a) low magnification image of the border of the mold (dashed line) and elongated crystals (arrows); b) higher magnification image of deposited material around the asterisk.

In general, the infiltration and crystal growth behavior observed for patterns of the network-like channel category were similar, with elongated crystals growing inside the pattern, as seen in the pattern of squares in Figure 6b, or from the edge of the pattern, as seen in in pattern of asterisks in Figure 7a. In the latter case, it seems that the crystals growing from the surplus of solution just outside the pattern disturbed the conformal contact between PDMS and Si substrate at the edge of the mold; this may explain the empty spaces between them, that can

18

be caused by trapped air (suggested by the rounded shape, typical of an air-liquid interface) and the absence of asterisk shapes on the crystals, that are otherwise observed in the center of the mold. In the center, elongated crystals are surrounded by a less organized phase or empty spaces, but these do not seem to show characteristics of trapped air bubbles, as seen at the edge.

Penetration of the solution in the patterns was poor, only 2 mm in the pattern square, which had a total length of 8 mm, and this was also the case for other geometries (not shown). The asterisk pattern was completely infiltrated but was smaller, with length around 5 mm, and infiltration was possible on all four sides of the mold, which was not the case for the square patterns, where the solution could only enter via two opposing sides. Moreover, the observed crystal growth seemed to be independent of the pattern features, in the sense that neither geometry could influence the growth of crystals at the macroscopic scale.

### 3.1.2. Infiltration of longitudinal channels

For addressing infiltration behaviour along patterns consisting of long and narrow parallel channels, a pattern of parallel lines with a length of 8 mm and variable width (ranging from 1 to 80 µm) was used, for which the respective PDMS mold (cast from the Si master from Figure 5c) and substrate were plasma treated for 1 min.
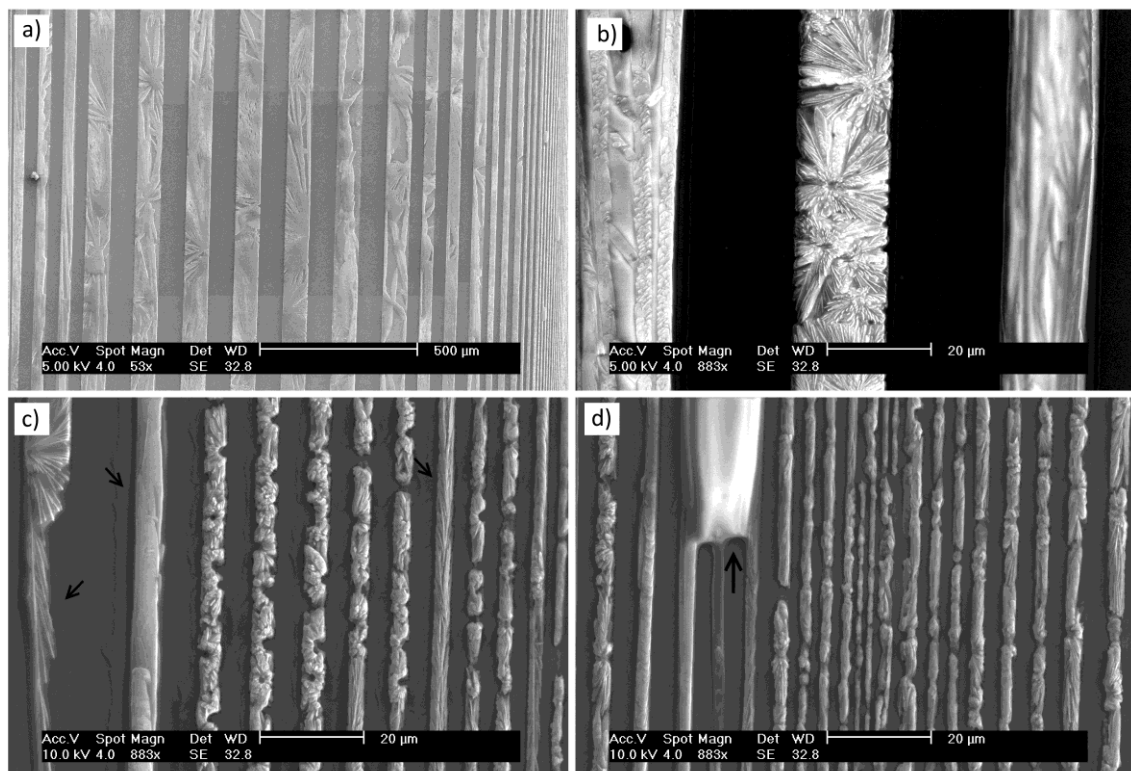


Figure 8. SEM micrographs of a CaP pattern of parallel lines with different widths: 80, 40, 20, 10, 5, 4, 3, 2 and 1 µm; a) low magnification overview of the central region of the mold, central lines are 80 µm wide; b) higher magnification image of 20 µm lines, flower-like crystals in the central line; c) 5 and 4 µm lines, arrows point to channels with elongated branching crystals; d) 4 to 1 µm lines, arrow points to a PDMS residue.

No infiltration front was observed in the central region of the mold, even in the smaller channels, showing that infiltration was complete across the mold (Figure 8a). PDMS residues from peeling leftovers, such as the one on Figure 8d, were found in the smaller lines (1 to 5 μm). On closer inspection of the patterned lines, the crystal morphology was not homogeneous but sharply defined as radial nodes of elongated needle-like crystals that give the structural repeating units the appearance of a flower (Figure 8b). The size and distribution of these flower-like crystals varied greatly, without direct relation to channel width. For instance in Figure 8c flower-like crystals around 5 μm are visible in the channels, but channels of the same width were also found with elongated branching crystals growing longitudinally (arrows in Figure 8c).

The same crystal morphology was found in the pattern of Figure 9, consisting of parallel lines with side chambers, with total width of 45 μm, for which the PDMS mold (cast from the Si master from Figure 5d) was treated as before. Infiltration was complete, as can be seen in the central region shown in Figure 9a. In Figure 9b a region with many small flower-like crystals around 10 μm in diameter could be observed, but in Figure 9c a region similar to the latter presents only one node from where radial elongated crystals filled the rest of the channel, spanning lengths of hundreds of microns.
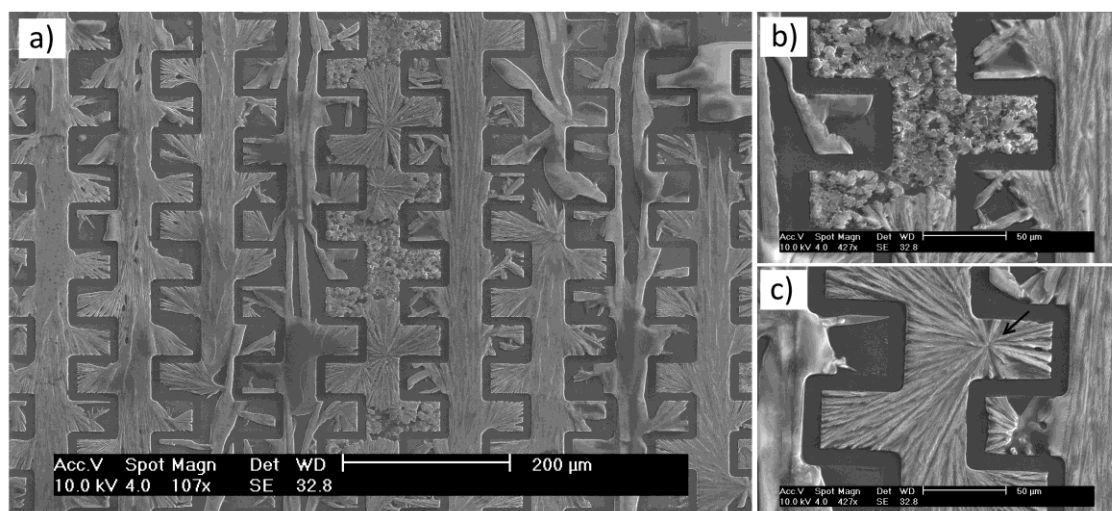


Figure 9. SEM micrographs of a pattern of parallel lines with side chambers (45 μm wide); a) low magnification image of the central region of the mold; higher magnification images show the crystal morphology to be either: b) flower-like crystals around 10 μm or c) long elongated crystals branching radially.

The variance in morphology between regions of high nucleation density and limited crystal growth (Figure 9b) and regions of low nucleation density and extensive crystal growth (Figure 5c) could not be linked to the shape or length of the channel, and either behavior was observed throughout the mold with no prevalence in specific regions. For nucleation to occur, local ion concentrations must surpass the equilibrium concentration at saturation (Miller *et al*. 2010), and the main factor contributing to this is the rate of solvent diffusion through the PDMS or evaporation through the channel openings (Veldhuis *et al*. 2012), which could not be directly

related to general geometric characteristics of the mold or drying conditions. This behavior was observed for all patterns of parallel channels alike.

The differences observed for infiltration behavior between the interconnected network of channels and the longitudinal channels can be explained by the dynamics of fluid propagation in confined spaces. As the solution infiltrates by capillary forces, the speed of fluid propagation and ultimately the complete filling of the channels are dependent on geometric characteristics - such as channel width, height, length (Delamarche *et al*. 1998) - and also on surface characteristics such as functional groups (hydrophilic vs hydrophobic) and roughness (Yong-Hoon & Urisu 2011).

For parallel channels the medium velocity of fluid inside the channel is given by equation 1.

$$\bar{v} = \frac{C_g}{\eta} \frac{\Delta p}{l} \qquad\qquad 1$$

It is proportional to the pressure drop inside the channel, $\Delta p$ (equation 2), that in capillary flow conditions depends on the surface tension of the liquid, $\gamma$, the contact angles with the surfaces inside, and cross-section of the channel (height *a*, width *b*); inversely proportional to the length *l* of the channel; and to the viscosity $\eta$. The term $C_g$ contains the geometry of the channel and can be approximated by equation 3.

$$\Delta p = \gamma \left( \frac{\cos(\theta_{substrate}) + \cos(\theta_{PDMS})}{a} + \frac{2\cos(\theta_{PDMS})}{b} \right) \qquad\qquad 2$$

$$C_g \cong \frac{1}{8} \left( \frac{ab}{a+b} \right)^2 \qquad\qquad 3$$

It means that channels with larger cross sections infiltrate faster than narrow channels, which was the observed behavior for infiltration in longitudinal channels (Delamarche *et al*. 1998)

The wetting ability of the solution also plays a role, but as it was kept the same throughout the entire study, the only variables between patterns are the geometry and the plasma treatment. The term $C_g$ would be different for the interconnected network of spaces, so a different infiltration behavior can be expected as well.

While extending the time of air plasma to the PDMS mold will make it more hydrophilic, it will also increase the strength of the bond between PDMS and substrate, increasing the probability of tearing the PDMS during removal, as was observed for plasma treatments longer than 1 min.

Another disadvantage of the interconnected network type of channels is the small contact area between the PDMS and Si substrate, that makes the PDMS to Si contact easy to disturb (since the bonding is not permanent) by crystals growing from the surrounding excess of

solution around the mold, which was seen for the asterisk pattern in Figure 7a. Coupled to the poor infiltration results, this led to the selection of longitudinal channels for further characterization of the deposited material, regarding the composition of the crystalline phase, the confinement of material to the pattern, ion release and cell compatibility.

## 3.2. Identification of crystalline phase

X-ray diffraction was used to identify the crystalline phase present in the CaP patterns, and to assess the effect of annealing. Two samples of 40 μm wide channels were prepared for this purpose; plasma treatment was for 1 min, and post-infiltration drying at 60 ℃ for 3 hours. One of samples received further heat treatment at 950 ℃ for 3 hours. The XRD patterns for the as-prepared (AP) and heat-treated (HT) samples are shown in Figure 10.
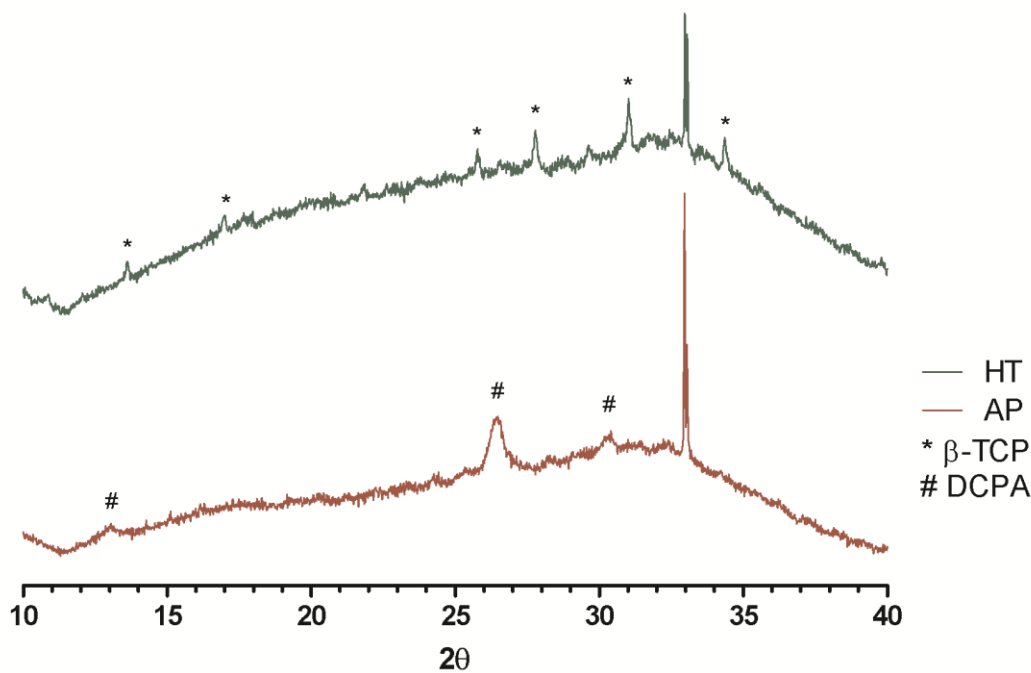


Figure 10. Diffraction patterns of two Si-CaP patterns of 40 um wide lines. Red: as-prepared (AP) sample; green: heat-treated (HT) sample; (#) indicates characteristic DCPA peaks, (*) indicates characteristic β-TCP peaks.

Peaks characteristic of dicalcium phosphate anhydrous (DCPA) were identified in the sample prepared without heat treatment (AP – as-prepared), specifically at 13º (001), 26.4º (double peak, 002 and 200) and 30.3º (120), and characteristic peaks of β-tricalcium phosphate (β-TCP) in the heat-treated sample (HT), at 13.6º (104), 17.0º (110), 25.8º (1010), 27.8º (214), 31.0º (0210) and 34.3º (220) (Figure 10). The sharp peak at 33º corresponds to silicon and originates from the substrate.

The formation of DCPA from a supersaturated solution with ethanol as solvent (Tas 2009), and the phase change of DCPA into β-TCP by annealing at 900-1000 ℃ (Eshtiagh-

Hosseini *et al.* 2008) have been reported before. Our data illustrates that the precipitation method used, in combination with relevant heat treatment can be employed to produce different CaP phases from the same solution. Further investigation into different heat treatments may be interesting, since, for instance, hydroxyapatite has been obtained from DCPA by heat treatment between 300 and 500 ºC (Lopatin *et al.* 1998).

## 3.3. Ion release and structure stability

Calcium phosphates have different solubility depending on the crystalline phase, for instance, DCPA has a solubility that is 9 to 10 times higher than that of β-TCP (Dorozhkin 2013). Release of calcium and phosphate ions in physiologic conditions and subsequent re-precipitation of carbonated apatite with incorporated biomolecules has been proposed to explain the bioactivity and osteoinductivity properties of CaP materials (Barradas *et al.* 2011). To evaluate the release potential of the Si-CaP substrates, calcium and phosphate ion release was measured for samples with two different geometries, 4 or 40 μm wide lines and two crystalline phases, DCPA and β-TCP, to investigate whether patterning or crystalline phase has any influence on dissolution. Ionic concentration was measured in cell culture medium, to test if there was dissolution of calcium phosphate to significantly alter ionic concentration of calcium or phosphate in cell culture conditions. Release profiles are shown in Figure 11.
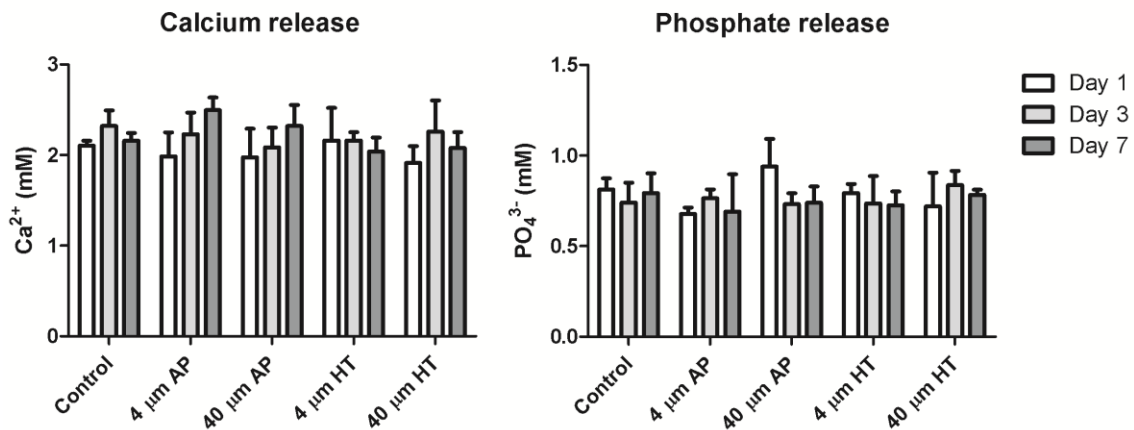


Figure 11. Calcium (left) and phosphate (right) concentration (mM) measured in incubation medium for 4 different samples over a period of 7 days. AP: as-prepared, corresponds to DCPA; HT: heat-treated, corresponds to β-TCP. Control was incubation medium.

No significant changes were found in the concentration of either calcium or phosphate in the incubation medium, for the three timepoints, and independently of geometry or heat treatment.

Since DCPA and β-TCP have different solubilities, a difference in concentration would be expected at least for the as-prepared and heat-treated samples, independently of geometry. The fact that no significant difference in concentrations were observed points to the possibility

that the amount of calcium phosphate material on the substrates was too small to significantly alter the ionic concentration in 1.5 mL of incubation medium, the volume used for cell culture. Furthermore, it is also possible that small changes in ionic concentration could not be determined by the method used, since the incubation medium itself possesses relatively high calcium and phosphate concentrations of 2.09 mM and 1.05 mM, respectively[2]. Eventually, for better characterization of ion release a more reliable quantification could be made in de-ionized water, with less working volume.

## 3.3.1. Structural stability

In order to evaluate morphology alterations due to the dissolution process, SEM micrographs of Si-CaP substrates were taken before and after ageing in cell culture medium for 3 days (Figure 12).
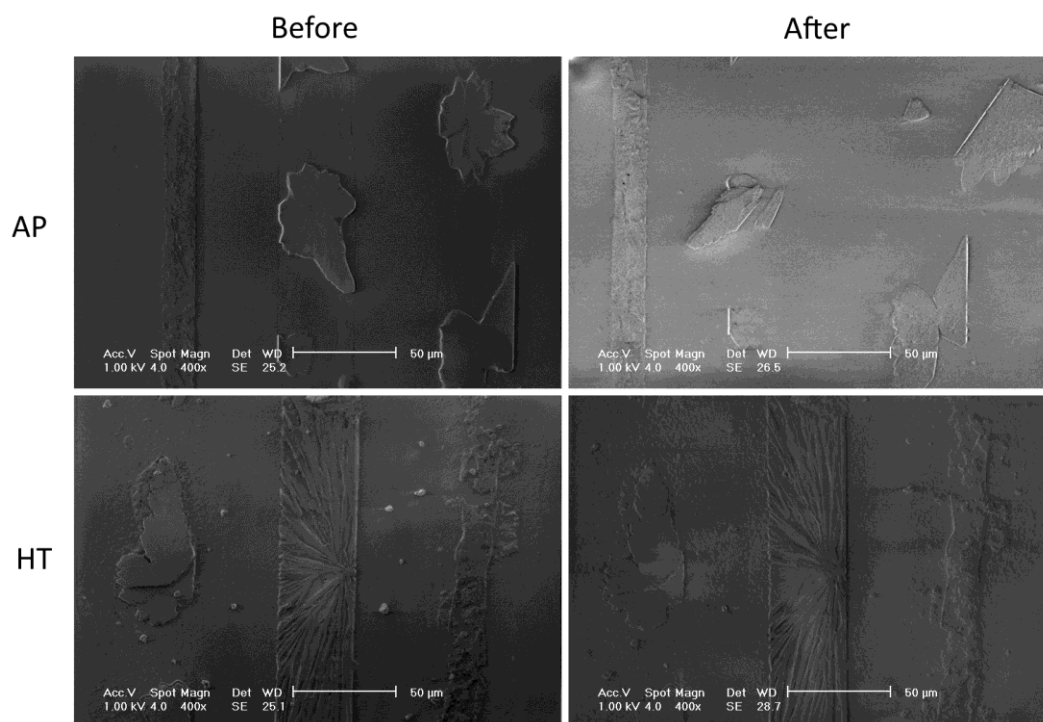


Figure 12. SEM micrographs of as-prepared (AP) and heat-treated (HT) Si-CaP substrates before and after ageing in cell culture medium for 3 days.

The as-prepared sample showed significant alteration of the observed area, which was unlikely to be caused by significant dissolution, as other areas imaged did not show similar alterations. It is more likely that the broken and detached crystals result from handling of samples during sterilization and medium.

---

[2] Calculated based on the medium specifications provided by Gibco, Life Technologies and on the measurements of fetal bovine serum provided in protocols of calcium and phosphate quantification kits from BioAssays Systems.

The heat-treated sample did not show signs of crystal detachment or other alterations, as observed for the as-prepared sample. This might suggest that the β-TCP patterns have better structural stability due to the heat treatment.

## 3.4. Elemental analysis

Elemental mapping of calcium and phosphorus by electron dispersive spectroscopy (EDS) was performed to check the reliability of the patterning method concerning the confinement of the deposited material inside the channels, for both as-prepared and heat-treated samples. Figure 13 shows SEM micrographs and EDS mapping of Ca and P for a pattern of 80 μm wide lines, prepared as described for the previous analysis. Both Ca and P were found exclusively inside the channels defined by the PDMS mold and the Si substrate, before and after heat treatment. Calcium was homogeneously distributed in the channels of both as-prepared and heat-treated samples. A similar, homogenous distribution of phosphorus was also observed in as-prepared sample, however, in heat-treated one, phosphorus distribution followed the morphology of the crystals, as observed in the SEM image (Figure 13).
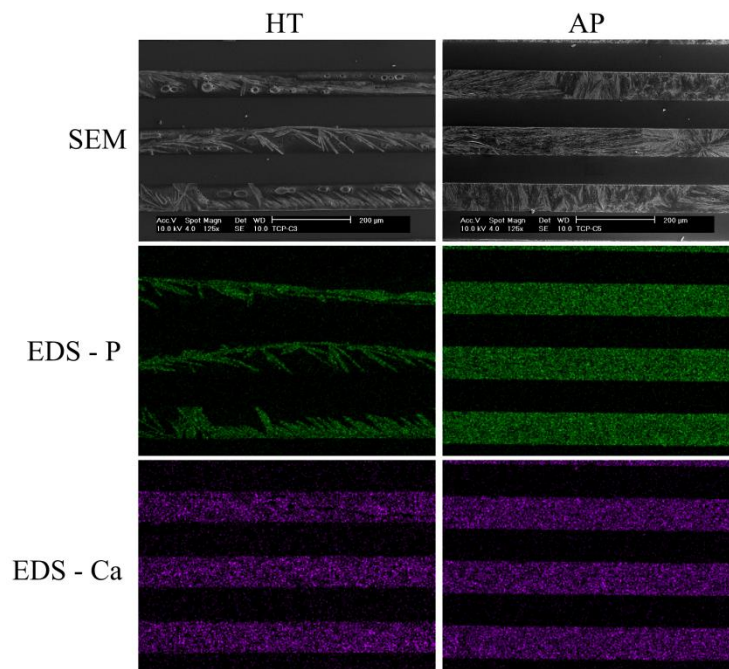


Figure 13. SEM micrographs and EDS mapping of calcium (pink) and phosphorous (green) for 80 μm wide channels before (AP) and after (HT) heat treatment.

The confinement of Ca and P to the channels confirmed that this patterning method is suitable for the deposition of geometrically defined calcium phosphates, as no distortion of the pattern defined by the PDMS can be seen. The discrepancy observed in the heat-treated sample, regarding the different distributions of Ca and P, can be attributed to the heterogeneity in crystal morphology already observed in the SEM images of optimization of infiltration, in such a way that crystals form along the patterns but not always completely fill the channel. The observed element distribution suggests that while phosphorus was mainly incorporated in the crystal

lattice, calcium was abundant and either adsorbed on the surrounding areas or formed a phase other than calcium phosphate. The latter is less likely due to the XRD pattern produced by the heat-treated samples, which show exclusively β-TCP peaks (Figure 10).

## 3.5. Cell culture

As mentioned previously in the Introduction, cell behavior strongly depends on surface chemistry and topography characteristics such as functional groups and surface charge, structures at micro or nano scale, roughness and degree of organization (Anselme *et al*. 2010). The Si-CaP substrates prepared here present topographical and chemical cues to the cells, through their geometrically patterned crystal morphologies and presence of calcium phosphates.

Osteoblast-like cells MG-63 were selected to investigate the behavior of cells on the Si-CaP substrates, and attachment, morphology, proliferation and ALP expression were assessed.

### 3.5.1. Biocompatibility and proliferation

Cell viability and proliferation assays were performed to validate biocompatibility of the Si-CaP substrates for cell culture. Viability was verified by quantifying metabolic activity with the Presto Blue® assay for 3 timepoints (day 1, 3 and 7) (Figure 14a), and proliferation by quantifying DNA with the CyQUANT® assay, for the same timepoints (Figure 14b). Substrates used were Si-CaP, heat-treated, with patterns of lines of varying width (5, 20 and 80 μm), and tissue culture plastic (TCP) was used as a control.
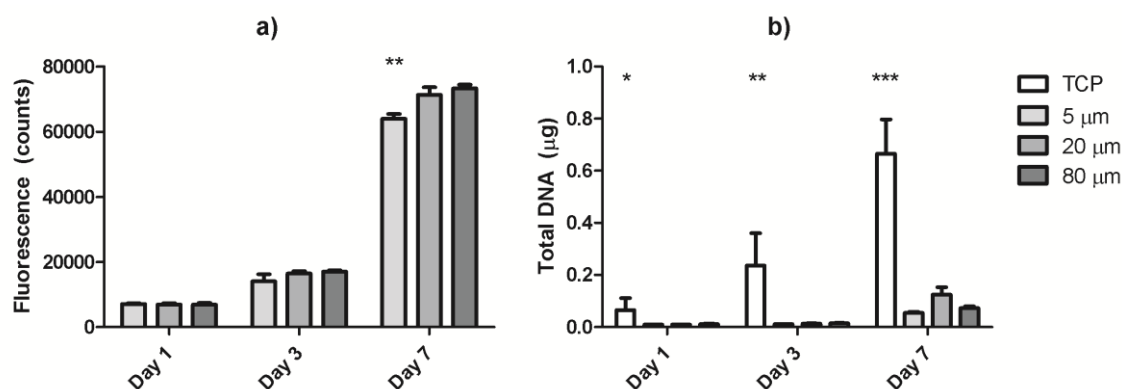


Figure 14. a) Total metabolic activity and b) total DNA content of MG-63 cells cultured on Si-CaP substrates with different line width (5, 20 and 80 μm). Control for DNA quantification was tissue culture plastic (TCP). Quantification was made after 1, 3 and 7 days of incubation.

Metabolic activity increased over time for all samples until day 7, without significant differences between samples, except at day 7 for the 5 μm lines, which exhibited lower metabolic activity than the other two geometries. The amount of total DNA was very low for the three Si-CaP substrates for day 1 and day 3 (without significant difference between them), with a visible increase at day 7 (6 to 7 times higher than day 3), but still well below the TCP control.

The amount of DNA increased from day 1 to day 7 for TCP control and was always significantly higher than that of Si-CaP substrates.

These data show that the proliferation of cells was negligible from day 1 to day 3, while metabolic activity doubled. From day 3 to day 7 there is noticeable proliferation coupled with increased metabolic activity. The low proliferation between the first two timepoints could mean that attachment and adhesion was hindered on the Si-CaP substrates, since there was a sevenfold difference in DNA amount between TCP and Si-CaP at the first day, it is plausible that a large number of cells were lost upon seeding.

Further investigation of the attachment and morphology of cells at day 1 and day 3, by SEM and fluorescence imaging, may help improve understanding these data.

### 3.5.2. Osteogenic profiling

Osteogenic profiling was assessed by quantification of alkaline phosphatase (ALP), an enzyme considered to be an early marker of osteogenic differentiation (Aubin 2001). Quantification was performed with CDPstar® reagent, on the same samples as used for DNA quantification, and the results are presented in Figure 15.
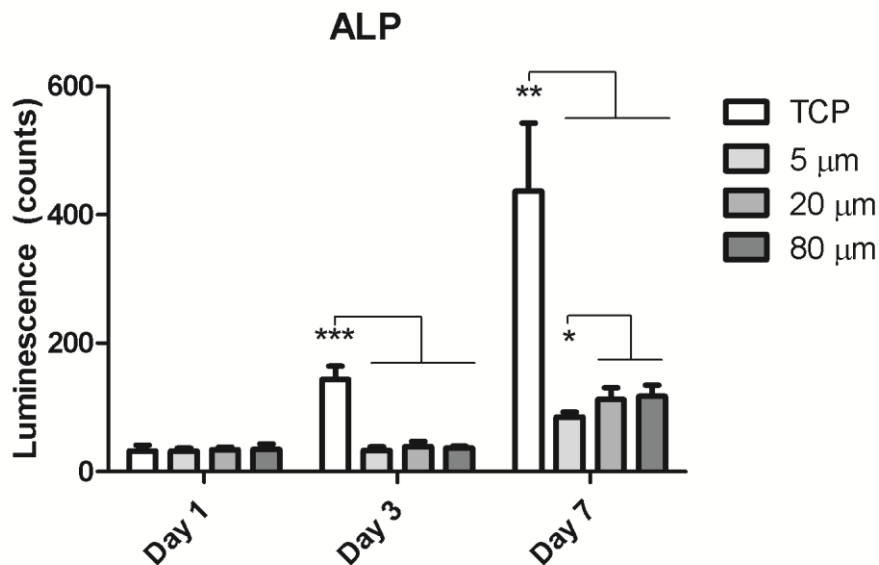


Figure 15. Total ALP amount of MG-63 cells cultured on Si-CaP substrates with different line width (5, 20 and 80 μm). Control was tissue culture plastic (TCP). Quantification was made after 1, 3 and 7 days of incubation.

All Si-CaP samples showed comparable ALP levels on day 1 and 3. Between day 3 and day 7, the 5 μm geometry showed a two-fold increase, while the other two geometries showed a three-fold increase. All geometries showed values comparable to the control on day 1, while on days 3 and 7, the ALP levels in all Si-CaP samples were about 4 times lower than on TCP.

The ALP data seemed consistent with the findings for DNA amount for all timepoints, therefore suggesting that the observed increase in ALP is due to the proliferation of cells, and

not to an increase in expression. There is a slight exception of TCP control not showing significant differences compared to the Si-CaP samples on day 1, which was the case for DNA amount (Figure 14b). This might suggest increased ALP activity for the Si-CaP samples at day 1, if ALP normalized to DNA was to be considered, but it must be noted that also for ALP quantification the luminescence measured for all samples at day 1, and for the Si-CaP samples at day 3, is on average only 1.5 times higher than the luminescence measured for the blank control. For comparison, TCP on day 3 was 6 times that of the control. Given that values for fluorescence at the limit of detection were also observed for DNA quantification[3], it seems unreliable to conclude that ALP levels are higher for cells cultured on Si-CaP substrates. Much more likely, the low values obtained for both analyses suggest a low number of cells with corresponding ALP levels.

### 3.5.3. Cell attachment and morphology

Cell attachment and morphology were assessed after 1 or 3 days of culture on Si-CaP substrates that consisted of a pattern of lines with varying width, from 1 to 80 μm, by SEM and fluorescence imaging of nuclei, F-actin, vinculin and focal adhesion kinase (FAK).

SEM micrographs in Figure 16 show cells attached on narrow (1 to 10 μm) or wide (20 to 80 μm) lines, on day 1 and day 3. Lamellipodia (cytoplasmic plate-like protrusions of cytoplasm) and filopodia (small fibre-like protrusions from lamellipodia) were visible from day 1 (Figure 16b), an indication that cells attached and were adhering and spreading on the surface of the substrates (Anselme 2000). Cells were also observed on spaces between patterned CaP when the width was not sufficient to fully contain a spread cell (3 to 20 μm in Figure 16a, 14b and 14c), or on top of them when they were large enough (50 μm in Figure 16d). Most of the observed contact points were established with the patterned ceramic. Moreover, cells appeared more stretched and oriented parallel to the pattern on narrow lines (1 to 10 μm) than on wider lines (20 to 80 μm).

---

[3] Further information regarding the DNA and ALP low levels of fluorescence or luminescence, respectively, can be found in appendix 6.4.

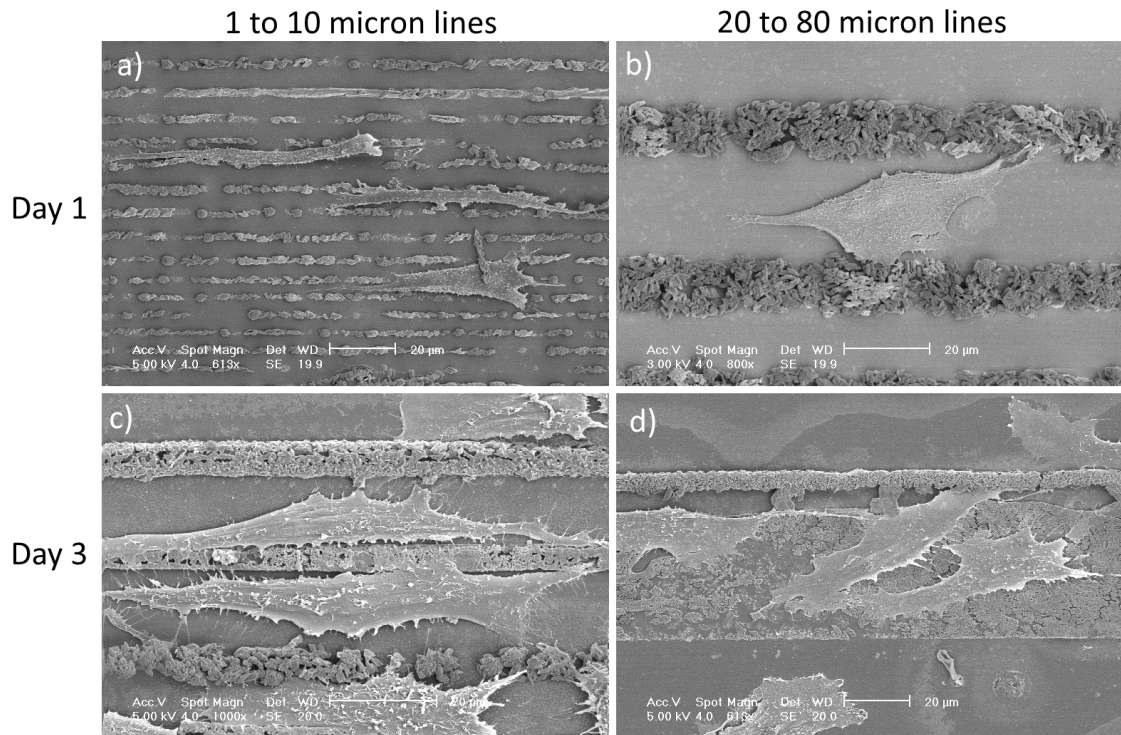**1 to 10 micron lines**   **20 to 80 micron lines**

Day 1

Day 3

Figure 16. SEM micrographs of MG-63 cells cultured on Si-CaP substrates for 1 (a,b) and 3 (c,d) days, for two different zones, narrow lines a) around 3 μm; c) around 6 μm;  and wider lines b) around 20 μm; d) around 50 μm.

The effect of cell alignment with the patterned lines seen on the SEM micrographs is more noticeable in the fluorescence images of nuclei and F-actin in Figure 17, where a larger area could be imaged. The stretching of the cells and the orientation of the major axis parallel to the direction of the patterned lines was more pronounced on the narrower patterns (1 to 10 μm) as compared to the wider patterns (20 to 80 μm), that presented more randomly oriented and less stretched cells. This as can be seen on day 1 (Figure 17a vs Figure 17b) and, when cell density is higher, on day 3 (Figure 17c vs Figure 17d).
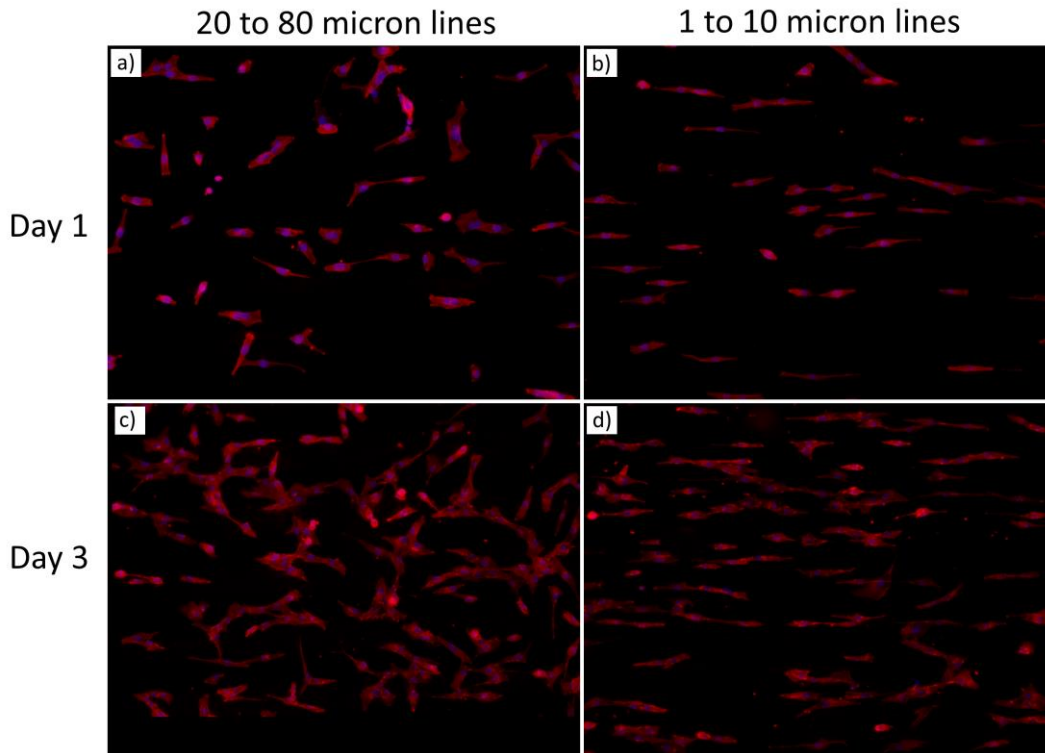
Figure 17. Fluorescence image of nuclei (blue) and F-actin (red) of cells cultured on Si-CaP substrates for 1 (a,b) or 3 (c,d) days; for two different regions: lines ranging from 20 to 80 μm (a, c) and lines ranging from 1 to 10 micrometers (b, d). Magnification of 10x.

This topography induced phenomenon, known as contact guidance, has been extensively reported for cells cultured on patterned microgrooves (Zheng *et al*. 2013; Prodanov *et al*. 2010; Nikkhah *et al*. 2012), and the higher degree of alignment for narrower lines here observed is in accordance with the results reported for a variety of cells and substrates (Biggs *et al*. 2008; Nikkhah *et al*. 2012).

Regarding the presented results of DNA quantification, that suggested lack of proliferation between day 1 and day 3, it should be noted that the analysis of several fluorescence images, of which the images from Figure 17 are representative, suggested proliferation of cells, although this was not quantified. This may suggest that the DNA assay performed was not reliable, and that quantification of cells based on image analysis may be a more suitable method in this case.

Vinculin and focal adhesion kinase (FAK) are two proteins associated with signal transduction from the focal adhesions to the cytoskeleton; they concentrate in mature focal adhesions that form upon contact of integrin membrane receptors with the substrate (Anselme *et al*. 2010; Anselme 2000). The immunofluorescence staining of vinculin and FAK in cells cultured on Si-CaP substrates are shown in Figure 18.
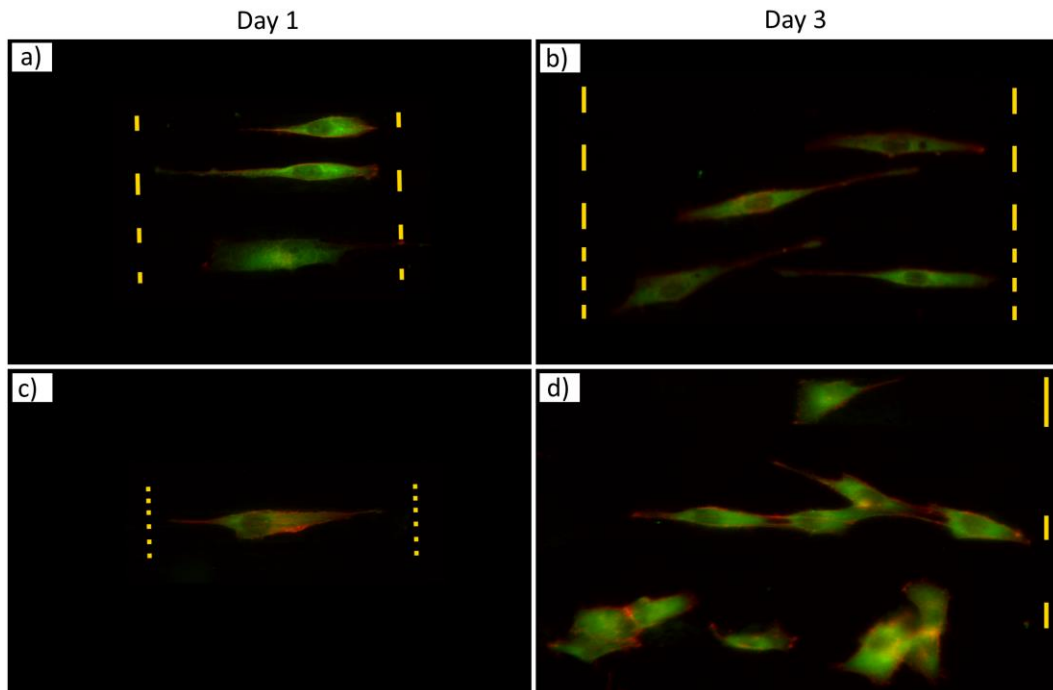
Figure 18. Fluorescence image of vinculin (green) and FAK (red) of cells cultured on Si-CaP substrates for 1 (a,c) or 3 (b,d) days; the yellow lines represent the underlying CaP pattern. Images are magnified 20 times.

Vinculin was found homogeneously distributed in the cytoplasm, without visible accumulation points. FAK was also found within the cell but with occasional higher intensity spots along the edges of the cells, mainly at day 3 (Figure 18d) possibly indicating that focal adhesions started to form at this point.

Assessment of attachment, spreading and adhesion by SEM and fluorescence imaging of F-actin, vinculin and FAK showed that cells were attached and showing signs of contact guidance already at day 1. This does not necessarily contradict the previously given statement that cell attachment and adhesion is hindered on Si-CaP substrates, since image analysis was solely qualitative in contrast to the DNA quantification.

## 3.6. Crystal growth dynamics

The ultimate objective of the patterning technique reported here is to achieve precise control over the topography and chemistry of the deposited material. As of now, moderate control over the chemistry has been achieved for two different calcium phosphates, DCPA and β-TCP, but the control over the micro- and nanostructure of the deposited material was only limited.

The heterogeneity in crystal morphology in the patterned material was already pointed out a number of times. In Figure 19, SEM micrographs of a 40 μm channel attest to that once again. In this case, all 4 images were taken from the same channel. The question arises as to why such differences in morphology occur over so short distances. How does it happen? Can it be controlled?
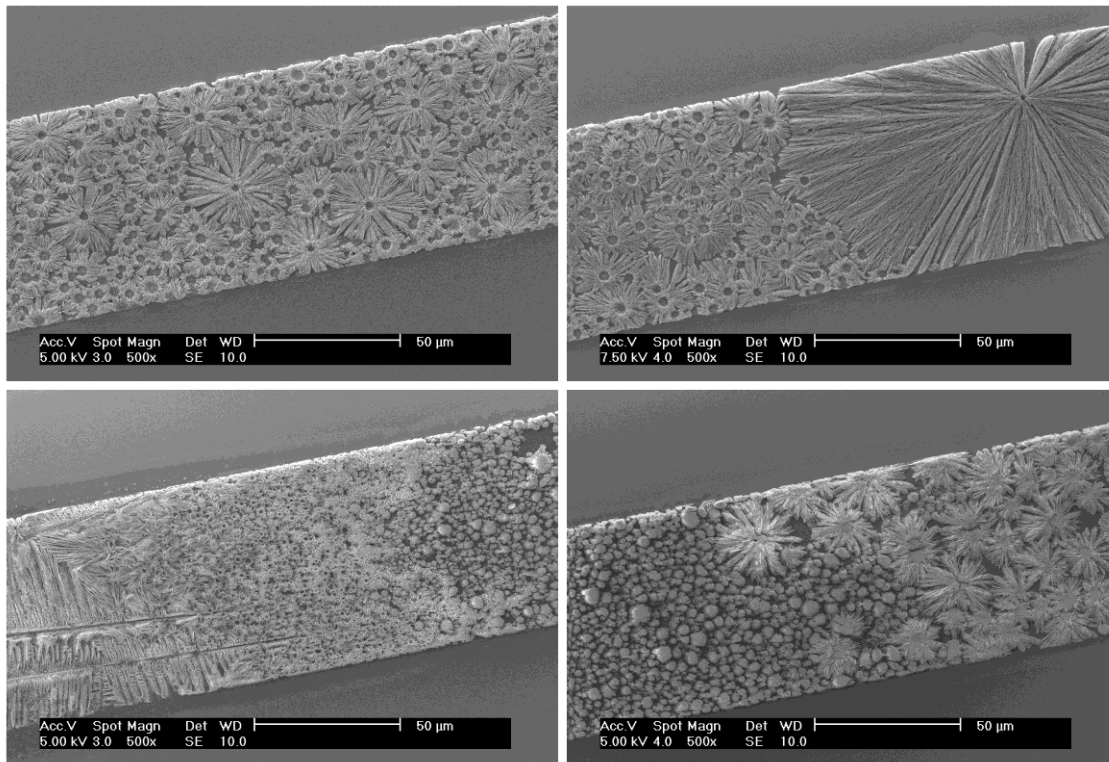


Figure 19. SEM micrographs of a 40 μm wide channel. Images are from the same channel, showing the different β-TCP crystal morphologies.

In an effort to understand the growth of crystals from the solution confined inside the channels, samples were prepared on glass substrates, instead of silicon, for imaging purposes. These were placed in a mini-incubator that allowed observation with an inverted microscope. Temperature was set at 37 °C and images were taken every 30 seconds. Figure 20 shows a few snapshots taken over a period of approximately 1 hour. Although the drying conditions were not the same as for the Si-CaP samples, due to the specifications of the incubator used, for the purpose of observing crystal nucleation and growth this presented no obstacle. Indeed, the

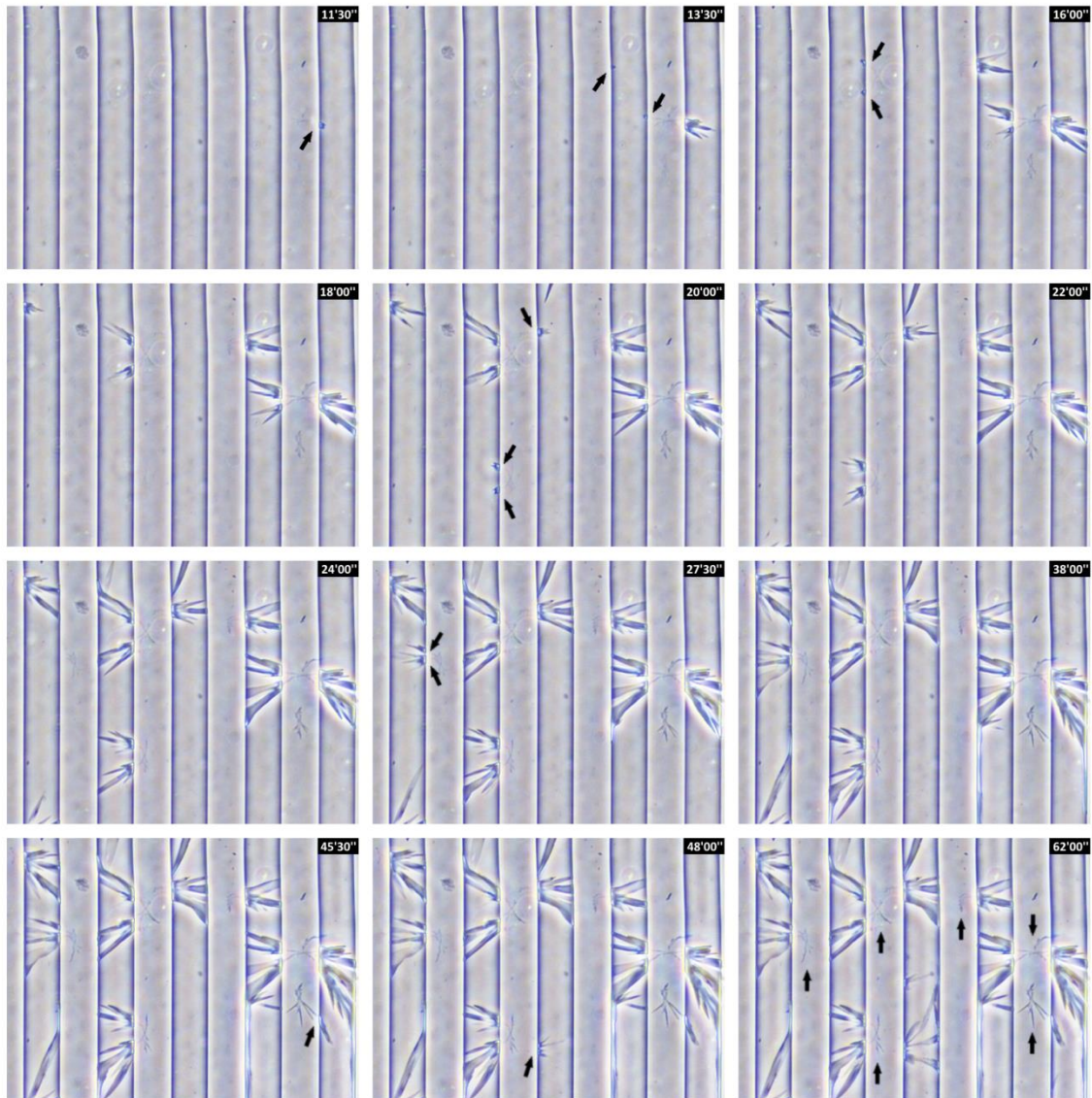crystal morphology appeared similar to the one found in previous samples, as can be seen below in Figure 20.



Figure 20. Snapshots of the timelapse crystal growth experiment. Channels are 80 µm wide. Time after infiltration is on the upper right corner of each image. Black arrows point the nucleation point of crystals, except on the last picture, where they point out the crystal growth between PDMS and glass.

As soon as 11 minutes after infiltration the first signs of nucleation were observed. Crystals seemed to start growing immediately upon formation of nucleation sites, represented by arrows in Figure 20, and continued to grow at the same time that new nucleation sites are formed. Upon nucleation, usually at the PDMS – glass corner of the channel, crystals grew with elongated branches in radial fashion, until encountering some obstacle, usually the opposing PDMS wall, that forces growth back in the direction of the channel.

One interesting feature can be seen in the last frame of Figure 20, where the arrows point to crystal growth that is not in channel, but instead where the PDMS should have been

bonded to glass. Inspection of the previous frames showed that this growth is already present before any crystals are seen inside the channels, and that the majority of crystals seem to grow from them. This suggests that nucleation started in spaces between the PDMS and the glass substrate, and crystal growth then proceeded to the channels filled with the ion-containing solution. A possible explanation is that some sort of imperfection in the PDMS to glass bond, caused by dust on the PDMS or a defect on the glass surface, allowed the infiltration of solution into this confined space, and nucleation was favored there over the larger channels due to more stable conditions. This may explain why many times it was observed that there crystals grew at the same "latitude" in adjacent channels, suggesting that crystal in both channels started growing from the same nucleation site located in the PDMS to glass interface between the two channels.

It must be noted that this effect was not observed in any samples with silicon substrate, where nucleation points, which were taken to be the centers of flower like aggregates of radial needle crystals, were always present inside the channel, as can be seen from the SEM micrographs of Figure 19. Nevertheless, this effect led to the concept of introducing geometrical defects as nucleation sites. If nucleation could be induced at these defined locations, then maybe a measure of control could be gained over the crystal morphology, to avoid the heterogeneity that is normally present in Si-CaP samples.

Further investigation of a method for controlling the nucleation sites was stopped due to lack of time, however, a number of options remains to be tested, such as different defect geometries or different etching profiles, that  may provide a more defined geometry and also increased roughness that might be desirable for the nucleation of crystals (Nijhuis *et al*. 2014).

# 4. CONCLUSIONS AND FUTURE PERSPECTIVES

The soft lithography derived method, based on the nucleation and growth of crystals from a supersaturated solution of calcium and phosphate ions infiltrated in microchannels, was successful in the patterning of calcium phosphate ceramics on a flat silicon substrate.

The infiltration of these channels by the solution was described for network-like channels and parallel channels. Infiltration on the parallel channels was complete for channel lengths up to 1cm, with 1 min plasma treatment on the PDMS mold and Si substrate. Radial nodes of elongated needle-like crystals were observed in the patterns, with heterogeneous distribution between two regions: one of high nucleation density and limited growth, other of low nucleation density and extensive growth. Further efforts should be made in order to obtain more control over the topography inside the channels, either by controlling nucleation, or by a method other than crystallization from a supersaturated solution.

Characterization of the crystalline phase in the longitudinal channels showed that the crystals grown were di-calcium phosphate anhydrous (DCPA), which upon heat treatment was converted in beta tri-calcium phosphate (β-TCP). The possibility of obtaining different calcium orthophosphates, such as hydroxyapatite (HA) or a mixture of HA and β-TCP, from the infiltration of the same solution upon applying different heat treatment is attractive because of its simplicity, and should be explored. Further characterization of the patterns should include quantification of the crystalline content and roughness measurements, and ion release quantification, eventually looking for an influence from geometry by testing different patterns.

Osteoblast-like cells MG-63 were cultured on the Si-CaP substrates and an increase of metabolic activity over the course of 7 days attested to the biocompatibility of the prepared substrates. However, it was observed that attachment of cells is hindered on the Si-CaP substrates when compared to standard tissue culture plastic, only a fraction of cells were present at day 1, as measured by DNA quantification. The amount of DNA found was so low as to put in question the reliability of the DNA quantification assay, and other methods of assessing proliferation should be looked into for validation, such as fluorescence based image analysis.

Fluorescence imaging showed that cells respond to the patterned lines by stretching and aligning with the direction of parallel lines. This effect was more noticeable in narrow lines (1 to 10 micron) than wider lines (20 to 80 microns), results that are in agreement with previous findings on the cell response on micropatterned grooves.

The adhesion of cells was further characterized by fluorescence imaging of focal adhesion proteins vinculin and focal adhesion kinase, and while vinculin showed dispersed presence in the cytoplasm, FAK was found concentrated on some points along the edge of cells at day 3, perhaps indicating the formation of focal adhesion complexes, predominantly at the edges of ceramic patterns.

Crystal growth in the channels was observed using a modified stand-alone mini incubator and time-lapse microscopy, and it proved itself as a promizing platform for observing crystal growth dynamics. In the experiment performed, atypical nucleation behaviour was found, with crystal nucleation as observed for Si-CaP substrates, but on the PDMS-glass interface. A proposed hypothesis is that a confined space was created by defects or particles at the PDMS-glass interface, and the solution infiltrated into such spaces, where more stable conditions would be favourable to nucleation of crystals.

A promising application of this platform could be studying the control of nucleation by the introduction of geometrically defined points where nucleation is favoured, either by etching the substrate to create confined spaces similar to the ones found at the PDMS-glass interface or by placing calcium phosphate seed points in the channels before infiltration of the solution.

# 5. REFERENCES

Anderson, J.M., 2001. Biological responses to materials. *Annual Review of Materials Research*, 31, pp.81–110.

Anderson, J.M., Rodriguez, A. & Chang, D.T., 2008. Foreign body reaction to biomaterials. *Seminars in immunology*, 20(2), pp.86–100.

Anselme, K., 2000. Osteoblast adhesion on biomaterials. *Biomaterials*, 21(7), pp.667–81.

Anselme, K. et al., 2000. Qualitative and quantitative study of human osteoblast adhesion on materials with various surface roughnesses. *Journal of biomedical materials research*, 49(2), pp.155–66.

Anselme, K., Ponche, A. & Bigerelle, M., 2010. Relative influence of surface topography and surface chemistry on cell response to bone implant materials. Part 2: biological aspects. *Proceedings of the Institution of Mechanical Engineers, Part H: Journal of Engineering in Medicine*, 224(12), pp.1487–1507.

Arima, Y. & A, H.I., 2007. Effect of wettability and surface functional groups on protein adsorption and cell adhesion using well-defined mixed self-assembled monolayers. *Biomaterials*, 28, pp.3074–3082.

Aubin, J.E., 2001. Regulation of osteoblast formation and function.pdf. *Reviews in Endocrine & Metabolic Disorders*, (2), pp.81–94.

Bala, Y. et al., 2011. Respective roles of organic and mineral components of human cortical bone matrix in micromechanical behavior: an instrumented indentation study. *Journal of the mechanical behavior of biomedical materials*, 4(7), pp.1473–82.

Bala, Y., Farlay, D. & Boivin, G., 2013. Bone mineralization: from tissue to crystal in normal and pathological contexts. *Osteoporosis international : a journal established as result of cooperation between the European Foundation for Osteoporosis and the National Osteoporosis Foundation of the USA*, 24(8), pp.2153–66.

Barradas, A.M.C. et al., 2011. Osteoinductive biomaterials: current knowledge of properties, experimental models and biological mechanisms. *European cells & materials*, 21, pp.407–429.

Biggs, M.J.P. et al., 2008. Adhesion formation of primary human osteoblasts and the functional response of mesenchymal stem cells to 330nm deep microgrooves. *Journal of the Royal Society, Interface / the Royal Society*, 5(27), pp.1231–42.

Bose, S., Roy, M. & Bandyopadhyay, A., 2012. Recent advances in bone tissue engineering scaffolds. *Trends in biotechnology*, 30(10), pp.546–54.

Brett, P.M. et al., 2004. Roughness response genes in osteoblasts. *Bone*, 35(1), pp.124–33.

Brown, B.N. & Badylak, S.F., 2013. Expanded applications, shifting paradigms and an improved understanding of host-biomaterial interactions. *Acta biomaterialia*, 9(2), pp.4948–55.

Bruinink, A. et al., 2013. Addition of nanoscaled bioinspired surface features: A revolution for bone-related implants and scaffolds? *Journal of biomedical materials research. Part A*, pp.275–294.

Cohen, J.E., 2003. Human population: the next half century. *Science (New York, N.Y.)*, 302(5648), pp.1172–5.

Dalby, M.J. et al., 2007. The control of human mesenchymal cell differentiation using nanoscale symmetry and disorder. *Nature materials*, 6(12), pp.997–1003.

Delamarche, E. et al., 1998. Microfluidic Networks for Chemical Patterning of Substrates : Design and Application to Bioassays. *Journal of the American Chemical Society*, 7863(2), pp.500–508.

Denis, A. et al., 2002. Protein Adsorption on Model Surfaces with Controlled Nanotopography and Chemistry. *Langmuir*, 75(19), pp.819–828.

Dorozhkin, S. V, 2010. Bioceramics of calcium orthophosphates. *Biomaterials*, 31(7), pp.1465–85.

Dorozhkin, S. V, 2013. Calcium Orthophosphate-Based Bioceramics. *Materials*, 6(9), pp.3840–3942.

Efremov, A.N. et al., 2013. Micropatterned superhydrophobic structures for the simultaneous culture of multiple cell types and the study of cell-cell communication. *Biomaterials*, 34(7), pp.1757–63.

Eshtiagh-Hosseini, H. et al., 2008. Preparation of anhydrous dicalcium phosphate, DCPA, through sol–gel process, identification and phase transformation evaluation. *Journal of Non-Crystalline Solids*, 354(32), pp.3854–3857.

Falconnet, D. et al., 2006. Surface engineering approaches to micropattern surfaces for cell-based assays. *Biomaterials*, 27(16), pp.3044–63.

Folch, A. et al., 1999. Molding of deep polydimethylsiloxane microstructures for microfluidics and biological applications. *Journal of Biomechanical Engineering*, 121(1), pp.28–34.

Fu, J. et al., 2010. Mechanical regulation of cell function with geometrically modulated elastomeric substrates. *Nature methods*, 7(9), pp.733–6.

Gao, C. et al., 2014. Current Progress in Bioactive Ceramic Scaffolds for Bone Repair and Regeneration. *International Journal of Molecular Sciences*, 15(3), pp.4714–4732.

George, A. et al., 2012. Micro and nanopatterning of functional materials on flexible plastic substrates via site-selective surface modification using oxygen plasma. *Journal of Materials Chemistry*, 22(2), p.328.

George, A. et al., 2011. Patterning functional materials using channel diffused plasma-etched self-assembled monolayer templates. *Langmuir*, 27(19), pp.12235–42.

Giselbrecht, S. et al., 2011. Closer to nature-bio-inspired patterns by transforming latent lithographic images. *Advanced materials*, 23(42), pp.4873–9.

Göbel, O.F., Blank, D.H. a & ten Elshof, J.E., 2010. Thin films of conductive ZnO patterned by micromolding resulting in nearly isolated features. *ACS applied materials & interfaces*, 2(2), pp.536–43.

Habibovic, P. & Groot, K. De, 2007. Osteoinductive biomaterials – properties and relevance in bone repair. *Journal of Tissue Engineering and Regenerative Medicine*, 1(1), pp.25–32.

Hamilton, D.W. & Brunette, D.M., 2007. The effect of substratum topography on osteoblast adhesion mediated signal transduction and phosphorylation. *Biomaterials*, 28(10), pp.1806–19.

Harink, B. et al., 2014. Microtiter plate-sized standalone chip holder for microenvironmental physiological control in gas-impermeable microfluidic devices. *Lab on a Chip*, 14(11), pp.1816–1820.

He, Y. et al., 2014. Preparation of hydroxyapatite micropatterns for the study of cell–biomaterial interactions. *Journal of Materials Chemistry B*, 2(16), p.2220.

Holthaus, M.G., Treccani, L. & Rezwan, K., 2011. Comparison of micropatterning methods for ceramic surfaces. *Journal of the European Ceramic Society*, 31(15), pp.2809–2817.

Hutmacher, D.W., 2000. Scaffolds in tissue engineering bone and cartilage. *Biomaterials*, 21(24), pp.2529–43.

Ingulli, E., 2010. Mechanism of cellular rejection in transplantation. *Pediatric nephrology*, 25(1), pp.61–74.

Kawano, T. et al., 2014. Honeycomb-shaped surface topography induces differentiation of human mesenchymal stem cells (hMSCs): uniform porous polymer scaffolds prepared by the breath figure technique. *Biomaterials Science*, 2(1), p.52.

Khan, S.U. & Elshof, J.E. Ten, 2012. Patterning titania with the conventional and modified micromolding in capillaries technique from sol–gel and dispersion solutions. *Science and Technology of Advanced Materials*, 13(2), p.025002.

Kieswetter, K. et al., 1996. Surface roughness modulates the local production of growth factors and cytokines by osteoblast-like MG-63 cells. *Journal of biomedical materials research*, 32(1), pp.55–63.

Kilian, K. a et al., 2010. Geometric cues for directing the differentiation of mesenchymal stem cells. *Proceedings of the National Academy of Sciences of the United States of America*, 107(11), pp.4872–7.

Kim, D.-H. et al., 2009. Mechanosensitivity of fibroblast cell shape and movement to anisotropic substratum topography gradients. *Biomaterials*, 30(29), pp.5433–44.

Kim, E. et al., 1997. Solvent-assisted microcontact molding: A convenient method for fabricating three-dimensional structures on surfaces of polymers. *Advanced Materials*, 9(8), pp.651–654.

Kim, E., Xia, Y.N. & Whitesides, G.M., 1995. Polymer microstructures formed by molding in capillaries. *Nature*, 376(6541), pp.581–584.

Kumar, A. & Whitesides, G.M., 1993. Features of gold having micrometer to centimeter dimensions can be formed through a combination of stamping with an elastomeric stamp

and an alkanethiol ink followed by chemical etching. *Applied Physics Letters*, 63(14), pp.2002–2004.

Lamers, E. et al., 2010. The influence of nanoscale grooved substrates on osteoblast behavior and extracellular matrix deposition. *Biomaterials*, 31(12), pp.3307–16.

Langer, R. & Vacanti, J.P., 1993. Tissue Engineering. *Science*, 260, pp.920–926.

Li, Y. et al., 2007. A method for patterning multiple types of cells by using electrochemical desorption of self-assembled monolayers within microfluidic channels. *Angewandte Chemie - International eddition*, 46(7), pp.1094–1096.

Lincks, J. et al., 1998. Response of MG63 osteoblast-like cells to titanium and titanium alloy is dependent on surface roughness and composition. *Biomaterials*, 19(23), pp.2219–32.

Liu, Y., Lim, J. & Teoh, S.-H., 2013. Review: Development of clinically relevant scaffolds for vascularised bone tissue engineering. *Biotechnology Advances*, 31(5, SI), pp.688–705.

Lloyd-Sherlock, P., 2000. Population ageing in developed and developing regions: implications for health policy. *Social science & medicine*, 51(6), pp.887–95.

Lopatin, C.M. et al., 1998. Hydroxyapatite powders and thin films prepared by a sol-gel technique. *Thin Solid Films*, 326(1-2), pp.227–232.

Matesanz, R., 2013. International Figures on Donation and Transplantation - 2012. *Newsletter Transplant*, 18(1), p.74.

McBeath, R. et al., 2004. Cell shape, cytoskeletal tension, and RhoA regulate stem cell lineage commitment. *Developmental cell*, 6(4), pp.483–95.

Miller, C., Komunjer, L. & Hlady, V., 2010. Heterogeneous nucleation of dicalcium phosphate dihydrate on modified silica surfaces. *Medicinski Vjesnik*, 42, pp.63–72.

Moller, K. et al., 1994. The influence of zeta-potential and interfacial tension on osteoblast-like cells. *Cells and Materials*, 4(3), pp.263–274.

Nadeem, D. et al., 2013. Embossing of micropatterned ceramics and their cellular response. *Journal of biomedical materials research. Part A*, 101(11), pp.3247–55.

Nijhuis, A.W.G. et al., 2014. Enzymatic pH control for biomimetic deposition of calcium phosphate coatings. *Acta biomaterialia*, 10(2), pp.931–9.

Nikkhah, M. et al., 2012. Engineering microscale topographies to control the cell-substrate interface. *Biomaterials*, 33(21), pp.5230–46.

Oliveira, S.M. et al., 2011. Chemical modification of bioinspired superhydrophobic polystyrene surfaces to control cell attachment/proliferation. *Soft Matter*, 7(19), p.8932.

Oliveira, S.M., Alves, N.M. & Mano, J.F., 2014. Cell interactions with superhydrophilic and superhydrophobic surfaces. *Journal of Adhesion Science and Technology*, 28(8-9), pp.843–863.

Olszta, M.J. et al., 2007. Bone structure and formation: A new perspective. *Materials Science and Engineering: R: Reports*, 58(3-5), pp.77–116.

Pelaez-Vargas, A. et al., 2013. Effects of density of anisotropic microstamped silica thin films on guided bone tissue regeneration--in vitro study. *Journal of biomedical materials research. Part B, Applied biomaterials*, 101(5), pp.762–9.

Peng, R., Yao, X. & Ding, J., 2011. Effect of cell anisotropy on differentiation of stem cells on micropatterned surfaces through the controlled single cell adhesion. *Biomaterials*, 32(32), pp.8048–57.

Place, E.S., Evans, N.D. & Stevens, M.M., 2009. Complexity in biomaterials for tissue engineering. *Nature materials*, 8(6), pp.457–70.

Prodanov, L. et al., 2010. The interaction between nanoscale surface features and mechanical loading and its effect on osteoblast-like cells behavior. *Biomaterials*, 31(30), pp.7758–65.

Rape, A.D., Guo, W.-H. & Wang, Y.-L., 2011. The regulation of traction force in relation to cell shape and focal adhesions. *Biomaterials*, 32(8), pp.2043–51.

Ratner, B.D. & Bryant, S.J., 2004. Biomaterials: where we have been and where we are going. *Annual review of biomedical engineering*, 6(1), pp.41–75.

Rho, J.Y., Kuhn-Spearing, L. & Zioupos, P., 1998. Mechanical properties and the hierarchical structure of bone. *Medical engineering & physics*, 20(2), pp.92–102.

Schweikl, H. et al., 2007. Proliferation of osteoblasts and fibroblasts on model surfaces of varying roughness and surface chemistry. *Journal of Materials Science: Materials in Medicine*, pp.1895–1905.

Seo, C.H. et al., 2011. A topographically optimized substrate with well-ordered lattice micropatterns for enhancing the osteogenic differentiation of murine mesenchymal stem cells. *Macromolecular bioscience*, 11(7), pp.938–45.

Seo, C.H. et al., 2013. The switching of focal adhesion maturation sites and actin filament activation for MSCs by topography of well-defined micropatterned surfaces. *Biomaterials*, 34(7), pp.1764–71.

Shegarfi, H. & Reikeras, O., 2009. Review article: bone transplantation and immune response. *Journal of orthopaedic surgery (Hong Kong)*, 17(2), pp.206–11.

Song, W., Kawazoe, N. & Chen, G., 2011. Dependence of Spreading and Differentiation of Mesenchymal Stem Cells on Micropatterned Surface Area. *Journal of Nanomaterials*, 2011, pp.1–9.

Tan, J.L. et al., 2003. Cells lying on a bed of microneedles: an approach to isolate mechanical force. *Proceedings of the National Academy of Sciences of the United States of America*, 100(4), pp.1484–9.

Tas, a. C., 2009. Monetite (CaHPO 4 ) Synthesis in Ethanol at Room Temperature. *Journal of the American Ceramic Society*, 92(12), pp.2907–2912.

Terris, B.D. et al., 1996. Nanoscale replication for scanning probe data storage. *Applied Physics Letters*, 69(27), pp.4262–4264.

Unadkat, H. V. et al., 2012. Correction for Unadkat et al., An algorithm-based topographical biomaterials library to instruct cell fate. *Proceedings of the National Academy of Sciences*, 109(15), pp.5905–5905.

Vacanti, J. & Vacanti, C.A., 2007. The history and scope of tissue engineering. In R. Lanza, R. Langer, & J. Vacanti, eds. *Principles of Tissue Engineering*. Elsevier, pp. 3–6.

Veldhuis, S. et al., 2012. Concentration dependence on the shape and size of sol-gel-derived yttria-stabilized zirconia ceramic features by soft lithographic patterning. *Langmuir*, 28(42), pp.15111–7.

Williams, D., 2008. Biocompatibility. In *Tissue Engineering*. Elsevier, pp. 255–278.

Williams, D.F., 2009. On the nature of biomaterials. *Biomaterials*, 30(30), pp.5897–909.

Woodruff, M.A. et al., 2012. Bone tissue engineering: from bench to bedside. *Materials Today*, 15(10), pp.430–435.

Xia, Y. & Whitesides, G.M., 1998. SOFT LITHOGRAPHY. *Annual Review Materials Science*, 28(12), pp.153–84.

Xia, Y.N. et al., 1997. Replica molding using polymeric materials: A practical step toward nanomanufacturing. *Advanced Materials*, 9(2), pp.147–149.

Yan, C., Sun, J. & Ding, J., 2011. Critical areas of cell adhesion on micropatterned surfaces. *Biomaterials*, 32(16), pp.3931–8.

Yao, X., Peng, R. & Ding, J., 2013a. Cell-material interactions revealed via material techniques of surface patterning. *Advanced Materials*, 25(37), pp.5257–86.

Yao, X., Peng, R. & Ding, J., 2013b. Effects of aspect ratios of stem cells on lineage commitments with and without induction media. *Biomaterials*, 34(4), pp.930–9.

Yong-Hoon, K. & Urisu, T., 2011. Casting mold patterning for lateral capillary force migration on PDMS microchannel. *Applied Surface Science*, 257(22), pp.9314–9317.

Yuan, H. et al., 2010. Osteoinductive ceramics as a synthetic alternative to autologous bone grafting. *Proceedings of the National Academy of Sciences of the United States of America*, 107(31), pp.13614–9.

Zhao, X.M., Xia, Y.N. & Whitesides, G.M., 1996. Fabrication of three-dimensional micro-structures: Microtransfer molding. *Advanced Materials*, 8(10), p.837–&.

Zheng, W., Zhang, W. & Jiang, X., 2013. Precise control of cell adhesion by combination of surface chemistry and soft lithography. *Advanced healthcare materials*, 2(1), pp.95–108.

# 6. APPENDIXES

## 6.1. Library of patterns

Figure 21. SEM micrographs of silicon masters of several available patterns to be replicated in PDMS and used in infiltration. Courtesy of Inorganic Materials Science group, University of Twente, Netherlands.
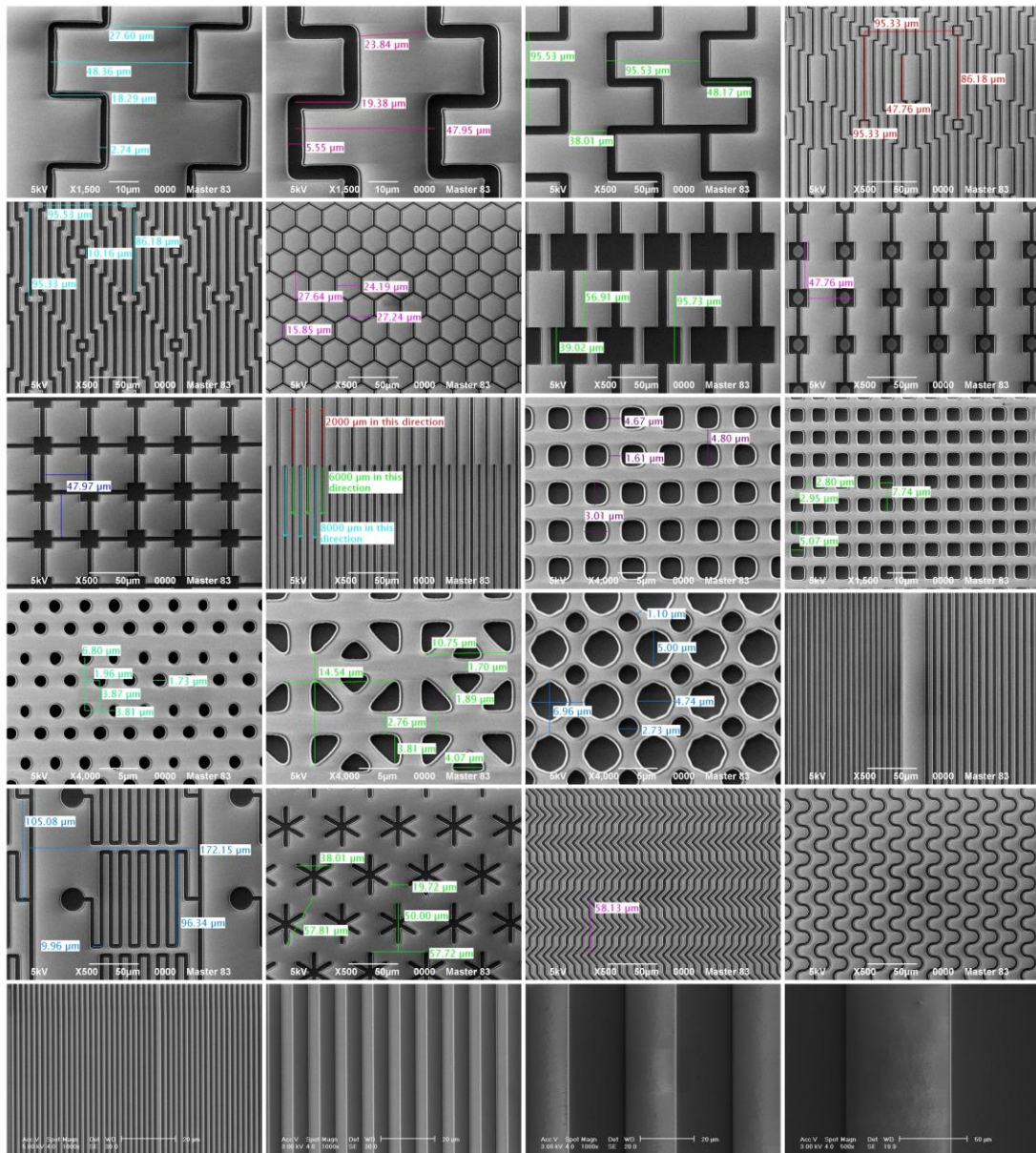
## 6.2. Attempted infiltrations

Table 3. Partial list of attempted infiltrations with different parameters.

| Sample name | Solution used | Mold | Plasma treatment | Drying | Heat treatment | Comment |
|---|---|---|---|---|---|---|
| A1 | Standard [Ca]=0.5M | 80 μm S | - | 25ºC 20, 60ºC 3h | 950ºC 3h 20ºC/min | Heterogeneous lines, needle-like crystals. |
| A2 | Standard [Ca]=0.5M | 80 μm S | - | 25ºC 20, 60ºC 3h | - | Heterogeneous lines, needle-like crystals |
| B1 | Standard [Ca]=0.5M | 40 μm L | Both 1min low | 25ºC 20, 60ºC 3h | 950ºC 6h 20ºC/min | Heterogeneous lines, needle-like crystals |
| B2 | Standard [Ca]=0.5M | 40 μm L | Both 1min low | 25ºC 20, 60ºC 3h | - | Heterogeneous lines, needle-like crystals |
| B3 | Standard [Ca]=0.75M | 40 μm L | Both 1min low | 25ºC wknd, 60ºC 4h, 80ºC | 950ºC 3h 20ºC/min | Solution precipitated befor infiltration, lines appear homogeneous before firing |
| B4 | Standard [Ca]=0.75M | 40 μm L | Both 1min low | 25ºC wknd, 60ºC | - | |
| C3 | [Ca]=0.25, PAA mw1800, MeOH, H$_2$O | 80 μm L | Sub 1min high | 25ºC overn. 85ºC 4h | 850ºC 1h, 20ºC/min | Filled channels, needle-like crystals, no PDMS stuck. |
| C5 | [Ca]=0.25, PAA mw1800, MeOH, H$_2$O | 80 μm L | Sub 1min high | 25ºC, 60ºC, 70ºC, 90ºC, 130ºC | - | - |
| C6 | [Ca]=0.25, PEG, MeOH, H$_2$0 | 80 μm S | Sub 1 min high | 25ºC, 60ºC, 70ºC, 90ºC, 130ºC | | Uniform film after 25ºC |
| D3 | [Ca]=0.25, PVP 25mg in 2mL sol | 80 μm S | Mold 2 min low | 25ºC 10h | - | Infiltration complete. PDMS stuck. |
| G3 | CPS | 80 μm S | Mold 30s low | 25ºC | - | Uniform coating, PDMS stuck.to substrate and material |
| G4 | CPS | 80 μm S | Mold 30s low | 60ºC | - | Uniform coating, PDMS stuck.to substrate and material |
| G5 | OCP | 80 μm S | Mold 30s low | 25ºC | - | Coating close to the walls |
| G6 | OCP | 80 μm S | Mold 30s low | 60ºC | - | Coating close to the walls |
| M2 | Hydrogel + triethylphosphate | 80 μm L | Sub 2 min high | 25ºC overn. UV cured 90min | 950ºC | Uniform coating |

## 6.3. Fluorescence spectra

Figure 22. Excitation and emission spectra of fluorophores used for staining. Emission spectrum of the mercury lamp used in the fluorescence microscope. Filters used for imaging of different fluorophores.
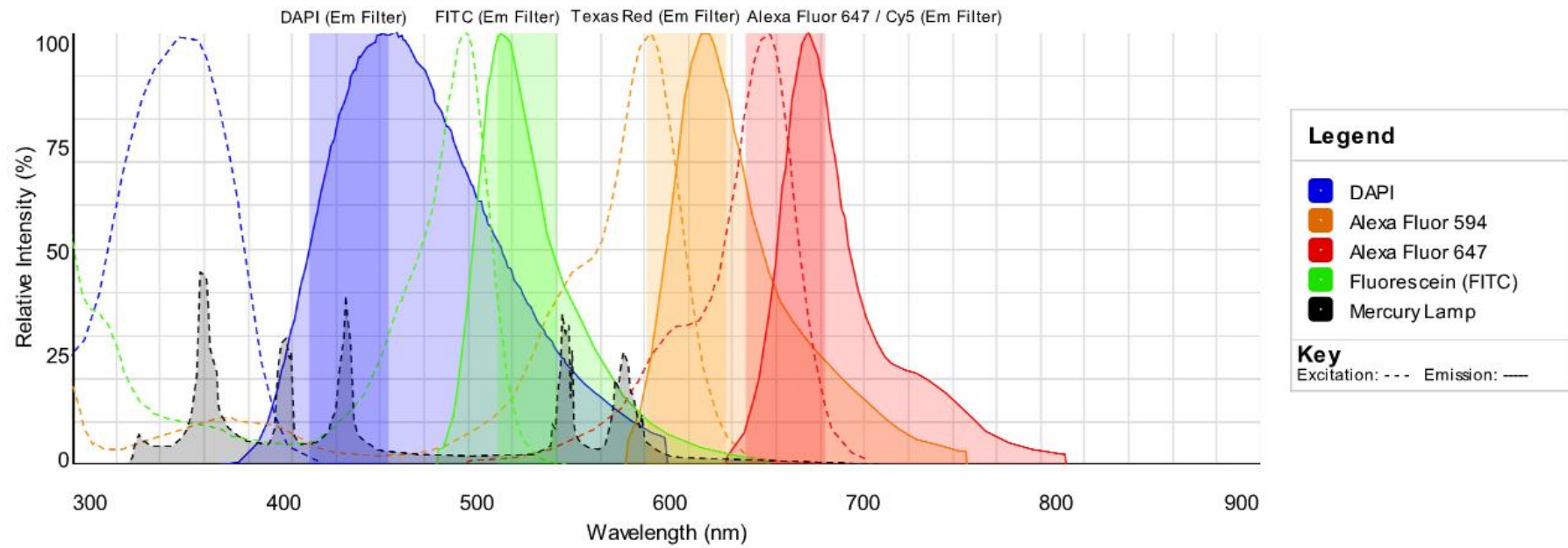
# 6.4. DNA and ALP supplementary graphics

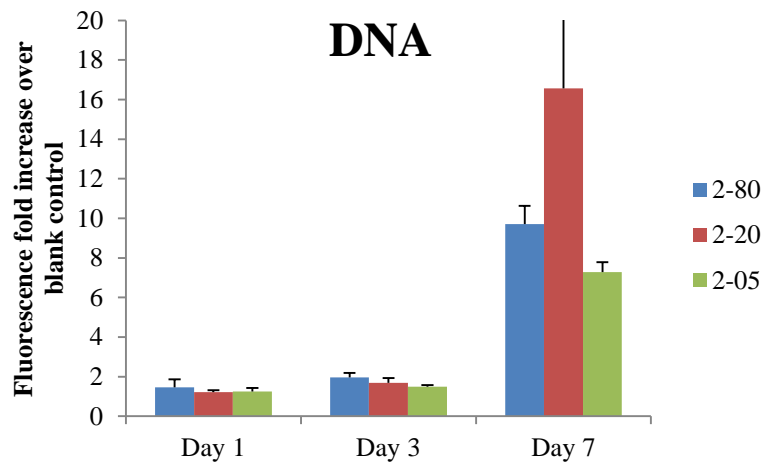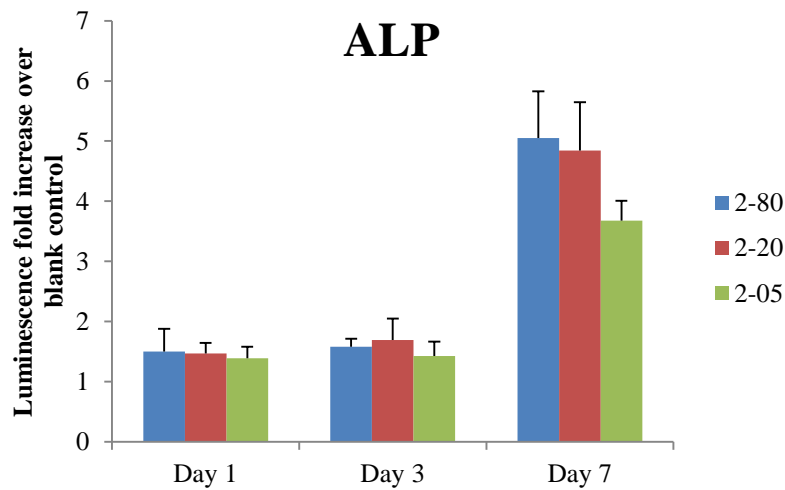Figure 23. DNA amount normalized to blank control.



Figure 24. ALP normalized to blank control.



Figure 25. ALP normalized to DNA.